Smooth band termination at high spin in ^{113}I

K. Starosta,* C. J. Chiara, D. B. Fossan, T. Koike, D. R. LaFosse, G. J. Lane,† J. M. Sears, and J. F. Smith‡
Department of Physics and Astronomy, State University of New York at Stony Brook, Stony Brook, New York 11794-3800

A. J. Boston, P. J. Nolan, E. S. Paul, and A. T. Semple
Oliver Lodge Laboratory, University of Liverpool, P. O. Box 147, Liverpool L69 7ZE, United Kingdom

M. Devlin§ and D. G. Sarantites
Department of Chemistry, Washington University, St. Louis, Missouri 63130

I. Y. Lee and A. O. Macchiavelli
Nuclear Science Division, Lawrence Berkeley National Laboratory, Berkeley, California 94720

I. Ragnarsson
Department of Mathematical Physics, Lund Institute of Technology, Box 118, S-22100 Lund, Sweden
(Received 27 July 2000; published 4 June 2001)

The ^{113}I nucleus has been studied using the ^{58}Ni(^{58}Ni,3p) reaction at 250 MeV with the Gammasphere/Microball facility. Gamma-ray three- and four-fold data gated by charged particle combinations were analyzed. Multipolarities of the γ rays were assigned following the angular correlation measurements. The present study is focused on the high spin properties, where the structure is dominated by $2p$-$2h$ excitations across the $Z=50$ gap. Ten decoupled bands showing the features of smooth band termination were observed; three of those bands are linked to known low-spin states, which allows the identification of configurations by direct comparisons with configuration-dependent cranked Nilsson-Strutinsky calculations. The yrast band, which was linked along with the signature partner, was followed up to $(101/2^+)$ and $\hbar\omega\sim 1.3$ MeV. The other linked band was a negative-parity band observed up to $(95/2^-)$. Tentative configurations for the unlinked bands are discussed. Comparisons with the theoretical results suggest that the band built on a configuration involving the neutron $i_{13/2}$ intruder orbital originating from the $N=6$ harmonic oscillator subshell was observed in this experiment.

DOI: 10.1103/PhysRevC.64.014304 PACS number(s): 21.10.Re, 23.20.Lv, 27.60.+j, 21.60.−n

I. INTRODUCTION

One of the long-standing topics in nuclear high-spin spectroscopy is the competition between collective and single-particle degrees of freedom. Collective models successfully describe the rotation of deformed nuclei with proton and neutron numbers sufficiently far from closed shells, while the single-particle shell model has a wide application for nuclei with proton and neutron numbers near closed shells. An interplay between these two extreme models is expected in transitional regions. The current paper reports on the wealth of structure information extracted from a high-spin study of the ^{113}I nucleus, which has three protons and ten neutrons outside the doubly closed ^{100}Sn core.

Nuclei near the $Z=50$ closed proton shell exhibit a novel collective structure that coexists with the expected single-particle structure. Intruder rotational bands have recently been observed in $Z=50$–52 nuclei up to high frequencies. These collective structures involve particle-hole ($2p$-$2h$) proton excitations across the $Z=50$ shell gap from the up-sloping high-K $\pi g_{9/2}$ orbital to the downsloping low-K $\pi g_{7/2}$ or $\pi h_{11/2}$ orbitals, which stabilize deformed prolate rotors. As the rotational frequency and spin increase for these intruder bands, the Coriolis interaction gradually aligns the valence particles resulting in characteristic decreasing dynamic moments of inertia and quadrupole transition moments; the observed unique excitation energy vs spin curves with subtracted rotating liquid drop reference (E-E_{LD}) depend on the specific configuration. These structure features have been interpreted using configuration-dependent cranking calculations, which show that as the available valence nucleons outside of the $Z=N=50$ double shell closure align, the nuclear shape gradually traces a path through the triaxial γ plane from a collective prolate shape ($\gamma=0°$) to a noncollective oblate shape ($\gamma=+60°$) over many transitions; this feature is called ''smooth band termination.'' After the available valence particles for a specific yrast configuration have aligned, the band sequence terminates at a spin that exhausts the sum of the aligned single-particle spins consistent with the Pauli principle. The smooth band termination phenomenon described above is now well established in the $A\sim 110$ region and recently has been reviewed in Ref. [1].

Since the success of these theoretical interpretations is

*On leave from: Institute of Experimental Physics, Warsaw University, Hoża 69, PL-00-681 Warsaw, Poland.

†Present address: Nuclear Science Division, Lawrence Berkeley National Laboratory, Berkeley, CA 94720.

‡Present address: Schuster Laboratory, University of Manchester, Manchester M13 9PL, United Kingdom.

§Present address: LANSCE-3, Los Alamos National Laboratory, Los Alamos, NM 87545.

related to the large shell gaps at $Z=N=50$, it is important to explore the smooth-termination band properties for different configurations that approach the yrast line as a function of an extended Z, N region. Thus the $Z=53$ I isotopes become important in this regard. The unique feature of the $A\sim110$ region relies on the fact that bands built on a specific microscopic configuration can be followed over a large spin and rotational frequency range; as an example for ^{113}I, band 1 is observed over a range of $38\hbar$ from spin $25/2^+$ and $\hbar\omega \sim 0.35$ MeV up to $(101/2^+)$ and $\hbar\omega\sim1.3$ MeV.

The ^{113}I nucleus is moderately deformed at low spin. At higher spin following the discussed $2p$-$2h$ proton excitations, larger deformations are achieved in the resulting $5p2h$ proton configurations. Ten bands built on these $2p$-$2h$ excitations are reported in the current study. Several of these structures in ^{113}I were first identified in Ref. [2]. The current study takes advantage of recent developments in experimental technique to substantially extend the previous results. The high sensitivity of the current experiment allowed observation of the linking transitions for three of the ten high-spin bands. For the states which form the linked bands, spins and parities can be reliably assigned. The experimental information on excitation energies, spins, and parities allows for direct comparisons with results of configuration-dependent cranked Nilsson-Strutinsky calculations discussed in Ref. [1]. Experimental data and theoretical calculations were found to be in excellent agreement for the linked bands. For the unlinked bands, spin assignments and microscopic configurations are proposed based on comparisons with the theoretical results. One of the observed bands fits very well with predictions for a configuration which involves the neutron $i_{13/2}$ orbital. The intruder $i_{13/2}$ orbital originates from the $N=6$ harmonic-oscillator subshell and is predicted in ^{113}I to approach the neutron Fermi level at high spin and rotational frequency. Neutron $i_{13/2}$ and proton $g_{9/2}$ orbitals are known to generate superdeformed shapes in the mass $A\sim130$ region. The current paper represents the first evidence of the neutron $i_{13/2}$ orbital in the $A\sim110$ region at neutron number $N=60$.

II. EXPERIMENTAL METHOD

Excited states in ^{113}I were populated following the ^{58}Ni(^{58}Ni,$3p$) reaction at a beam energy of 250 MeV. The experimental setup consisted of the Gammasphere array of 83 HPGe detectors [3] coupled with the Microball array of 95 CsI(Tl) charged-particle detectors [4], and an array of 15 scintillators for neutron detection. Neutron detectors were not used directly for the ^{113}I study, although they were essential in the analysis of other channels populated in the experiment which represented background (see Ref. [5] for ^{109}Te, Ref. [6] for ^{111}Te, and Ref. [7] for ^{110}I). In order to obtain γ-ray sum-energy and multiplicity information, the Hevimet collimators ordinarily placed in front of the Compton-suppression shields to reduce direct γ-rays were removed for this experiment as discussed in Ref. [8].

Two self-supporting ~500 μg/cm^2 stacked targets were used in the current study. The observed γ-ray energies were corrected off-line for Doppler shifts. The Doppler correction procedure involved event-by-event reconstruction of the momentum vector for the residual nuclei based on reaction kinematics and the measured charged-particle momentum vectors [4]. The average velocity of the recoiling nuclei was measured to be $\beta\sim4.5\%$ in agreement with the value calculated based on reaction kinematics. In the $3p$-gated channel, a γ-ray energy resolution of $\Delta E_\gamma\sim8$ keV full width at half maximum (FWHM) at $E_\gamma\sim1.3$ MeV was achieved for spectra used in the final analysis. The resolution was measured using the 1331-keV transition of band 2 in ^{113}I to compare with the value given in Ref. [2] (see discussion below) and with the intrinsic resolution of the Ge detectors measured with a ^{60}Co source.

For the off-line analysis, coincident events were sorted into charged-particle gated γ-γ matrices, γ-γ-γ cubes, and γ-γ-γ-γ hypercubes. The main part of the data analysis was carried out using the Gammasphere/Microball cube and hypercube both gated on three protons. The Microball efficiency for single proton detection measured in the present experiment was $\sim80\%$. It was observed that the $3p$ and the $2p$ gates contained $\sim50\%$ and $\sim40\%$ of the $3p$ channel statistics, respectively, in agreement with the estimate based on the binomial distribution. A cube including both the $3p$ and $2p$ gates was sorted and analyzed for the cases where statistics were needed. A $3p$-gated cube with additional gates on γ-ray multiplicity/sum energy and proton sum energy was also sorted with the gates optimized to reduce the $4p$ ^{112}Te channel leaking into the $3p$ gate. This cube was used for the cases where additional isolation was necessary. The γ-ray spectroscopy software package RADWARE [9] was used extensively for the data analysis.

A complementary experiment with a ~2 mg/cm^2 thick ^{58}Ni backed target and with the same reaction and beam energy as in the Gammasphere run was performed using the Stony Brook TANDEM/superconducting LINAC facility and a six Compton-suppressed Ge-detector array. This backed-target experiment provided γ-ray coincidence data with good energy resolution, $\Delta E_\gamma\sim2$ keV FWHM at $E_\gamma\sim1.33$ MeV, with the elimination of the Doppler effect. Spectra in the backed target experiment were recorded by detectors placed approximately at $\pm30°$, $\pm90°$, and $\pm150°$ with respect to the beam direction.

An angular correlation study [10] was performed for γ-ray multipolarity assignments. An asymmetric $3p$-gated matrix was sorted from the Gammasphere/Microball data with the detectors at $\theta>142°$ incremented on one axis and the detectors with $79°<\theta<101°$ on the other axis (note that the forward rings of Ge detectors were replaced by neutron detectors). A similar matrix was sorted using backed-target Stony Brook data. DCO ratios [10] extracted for known quadrupole-dipole and quadrupole-quadrupole cascades in ^{113}I [2] are $R_{DCO}=0.65(3)$ for the $15/2^-\rightarrow11/2^-\rightarrow9/2^+$ cascade and $R_{DCO}=0.99(5)$ for the $19/2^-\rightarrow15/2^-\rightarrow11/2^-$ cascade. When experimental DCO ratios of nondirect successive transitions were compared to the theoretical predictions the effect of unobserved transition was calculated following the formalism presented in Ref. [11] using the programs described in Ref. [12].

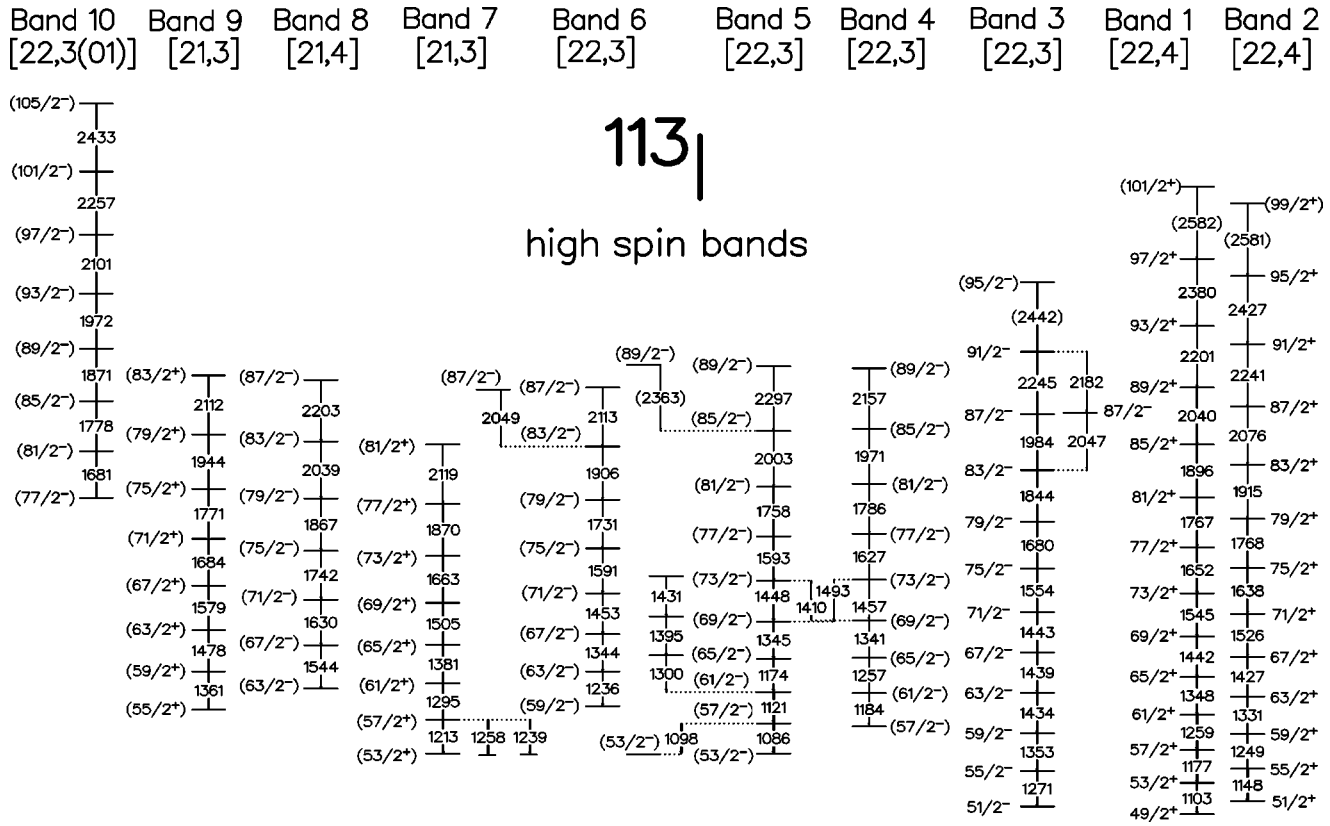

FIG. 1. Decoupled bands observed at high spin in ^{113}I. See text and Fig. 2 for the details of the spin assignments for linked bands 1–3. Spin assignments for unlinked bands 4–10 are based on a theoretical calculation.

In a number of cases, γ-ray energies measured in the current study differ from those reported in Ref. [2]. The discrepancy seems to be more pronounced for high-energy γ rays observed in the thin-target experiment. The energies measured in the current study are adopted as more reliable because of the improved resolution FWHM$\sim$8 keV at $E_\gamma \sim$1.3 MeV compared to the FWHM$\sim$10 keV reported in Ref. [2]; the good energy resolution in this thin-target experiment was achieved because of the improved Doppler correction procedure using the Microball array and the better angular granularity provided by the detector segmentation in the Gammasphere array.

III. EXPERIMENTAL RESULTS

Ten decoupled $\Delta I=2$ bands observed up to high spins in ^{113}I are shown in Fig. 1. Stretched $E2$ multipolarity for the intraband transitions is assumed following the rotational character of these bands. Experimental information presented in the current paper on states with spin $I \leqslant 55/2$ is limited to what is relevant for the discussion of the high-spin properties of ^{113}I. A partial level scheme of ^{113}I, showing the bands at low spin together with the linking transitions for bands 1, 2, and 3, is shown in Fig. 2. Information about energies, intensities, DCO ratios, proposed multipolarities of the γ-ray transitions, and spin assignments for excited levels in ^{113}I is summarized in Table I. Information about band intensities at $E_\gamma \sim$1.6 MeV is summarized in Table II. The details are discussed below.

A. Bands *a*, *b*, *y*, and *s*

The part of the ^{113}I level scheme including the one-quasiparticle band *y* and three-quasiparticle band *s* which form the yrast line in the low-spin region agrees with the results of the previous study [2]. The spins for the yrast states were adopted from the tentative assignment given in Nuclear Data Sheets [13] and systematics of the odd-A $_{53}$I isotopes [14]. These assignments are supported by the theoretical interpretation of the yrast bands in odd-A $_{53}$I nuclei at low excitation energy as being based on the low-K $\pi h_{11/2}$ orbital. These adopted spins are consistent with the results of the DCO analysis for the γ-ray transitions in bands *y* and *s*. The arguments listed above assign spin $11/2^-$ to the bandhead of band *y*.

Stretched $E1$ and stretched $E2$ multipolarity proposed in Ref. [2] for the 388-keV transition which depopulates the $11/2^-$ bandhead of band *y*, and subsequent 629-keV transition, respectively, are consistent with the results of the DCO analysis in the current study. These assignments imply $I^\pi = 5/2^+$ for the lowest-energy state observed in the experiment. This result agrees with the systematics of the ground-state spins for odd-A $_{53}$I isotopes, $I^\pi = 5/2^+$ for $N \leqslant 74$. The results of the current DCO analysis are also consistent with a stretched $E1$ multipolarity for the 180-keV transition depopulating the bandhead of band *y*, which results in a stretched $E2$ multipolarity for the subsequent 838-keV transition to the $5/2^+$ ground state.

The DCO ratio measured in the current backed target experiment for the 264-keV γ ray depopulating the $11/2^-$

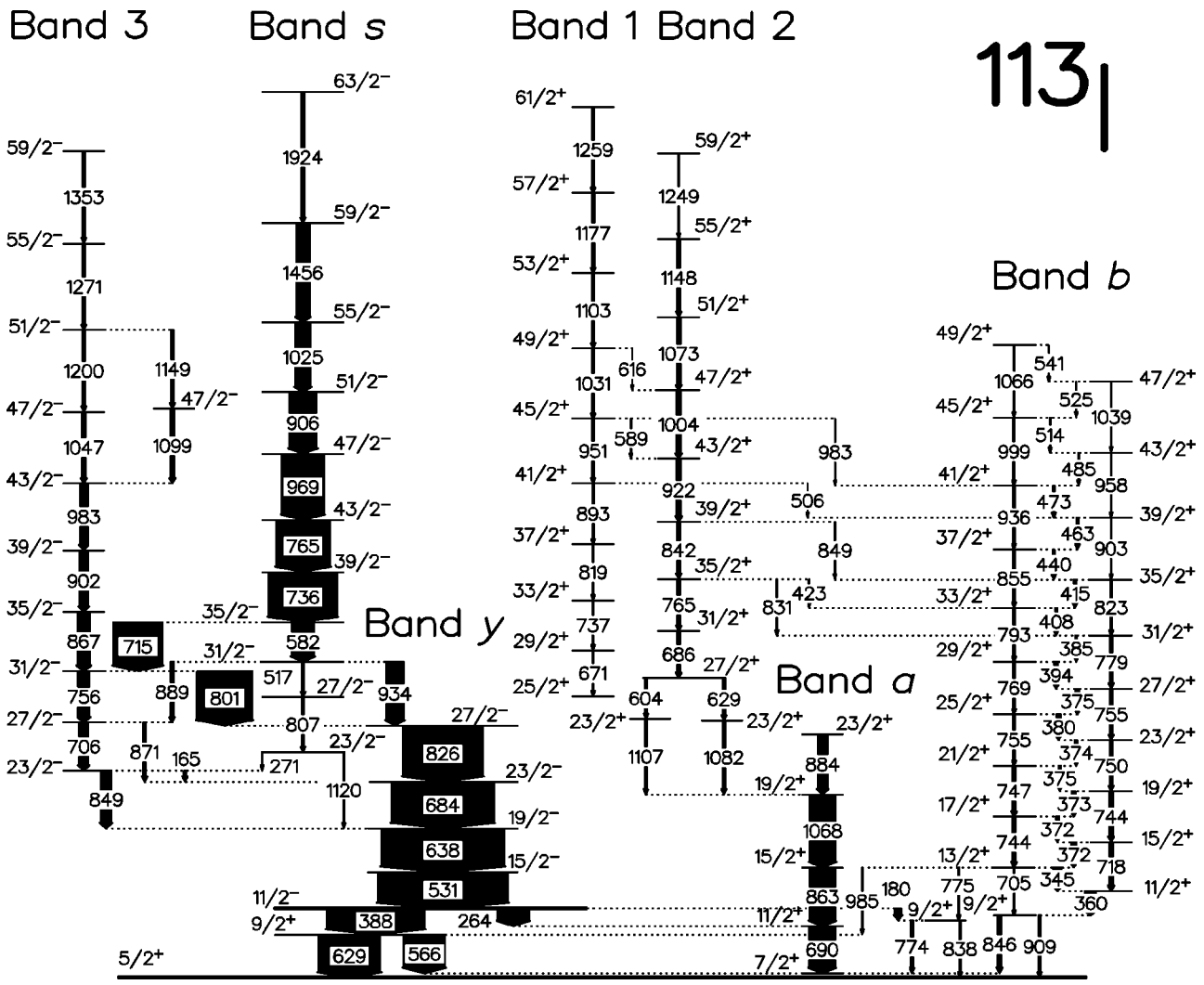

FIG. 2. Partial level scheme of ^{113}I at low spin/excitation energy. Proposed spin assignments are based on the DCO analysis and systematics of band structures in odd I isotopes.

bandhead of band *y* is consistent with an $I_i = I_f$ $E1$ multipolarity, rather than with the stretched $E1$ multipolarity of Ref. [2]. Therefore a $11/2^+$ assignment rather than $9/2^+$ is proposed for the first excited state of band *a*. The 753-keV transition reported in Ref. [2] between this state and the ground state was not observed in the current experiment. The DCO ratio for the 690-keV transition depopulating the $11/2^+$ state of band *a*, measured using a gate on the 531-keV transition of band *y*, is consistent with stretched $E2$ multipolarity for the 690-keV γ ray and spin $7/2^+$ for the bandhead of band *a*. DCO analysis for the 690-, 863-, and 1068-keV γ rays of band *a* performed using spectra from the thin-target experiment gated on the 884-keV transition yields stretched $E2$ multipolarity for all band members. Band *a* was not reported in Ref. [2], although a low-spin band built on the $(d_{5/2}g_{7/2})$ quasiproton was observed in heavier odd-*A* I isotopes, see Refs. [15] and [16] for ^{117}I and ^{119}I, respectively.

The other positive-parity band at low spin (band *b*) was reported in Ref. [2]; one should note, however, that the level scheme for this band in the current study (see Fig. 2) differs from that of Ref. [2]. The current level scheme follows the results of a four-fold analysis which indicates the existence of more dipole transitions in the energy range between 372 and 375 keV than the three γ rays of Ref. [2]. The spin $9/2^+$ was adopted for the bandhead following the tentative assignment given in Nuclear Data Sheets [13] and the systematics of odd-A $_{53}$I isotopes [14]. This assignment is supported by the theoretical interpretation of the corresponding bands in odd-A $_{53}$I isotopes at low spin as being built on the high-K $\pi g_{9/2}^{-1}$ orbital. The spins for the band members were assigned following the strongly coupled $\Delta I = 1$ character of the band, supported by the observation of the $E2$ crossover transitions; these assignments are further confirmed by the comparison with the systematics of corresponding bands in odd-A $_{53}$I isotopes [14]. The DCO analysis for the transitions of band *b* is hindered due the fact that many of the γ rays in the band are very close in energy and that the band was populated with less intensity than other bands at low spin. The DCO ratios for the group of the γ rays with energy $\sim$744 keV extracted from the gate set on $\sim 744-$keV transitions are consistent with the stretched $E2$ crossovers. The DCO ratios measured for the 345-, 360-, $\sim 373-$keV transitions in the

TABLE I. Results for γ-ray transitions in ^{113}I shown in Figs. 1 and 2.

E_γ (keV)	I_γ (%)	DCO ratio	I_i^π	→	I_f^π	Multipolarity	Band
165.1(0.5)	2.2(0.2)	0.86(8) [b]	$23/2^-$	→	$23/2^-$	$M1/E2$	3
179.8(0.5)	4.7(0.5)	0.65(6) [b]	$11/2^-$	→	$9/2^+$	$E1$	y
263.9(0.5)	23.9(0.9)	1.3(2) [a]	$11/2^-$	→	$11/2^+$	$E1$	y
271.0(0.6)	0.5(0.1)		$23/2^-$	→	$23/2^-$	$M1/E2$	s
345.4(0.5)	6.6(0.4)	0.73(6) [b]	$13/2^+$	→	$11/2^+$	$M1/E2$	b
360.0(0.5)	8.4(0.6)	0.74(6) [b]	$11/2^+$	→	$9/2^+$	$M1/E2$	b
372.0(1.0)	4.1(1.2)		15.2^+	→	$13/2^+$	$M1/E2$	b
372.4(1.0)	2.8(1.1)		$17/2^+$	→	$15/2^+$	$M1/E2$	b
373.0(1.0)	2.9(1.1)		$19/2^+$	→	$17/2^+$	$M1/E2$	b
374.0(1.0)	2.3(1.1)	0.75(5) [b]	$23/2^+$	→	$21/2^+$	$M1/E2$	b
375.0(1.0)	2.7(1.1)		$21/2^+$	→	$19/2^+$	$M1/E2$	b
375.4(1.0)	2.2(1.1)		$27/2^+$	→	$25/2^+$	$M1/E2$	b
380.0(1.0)	3.3(0.3)		$25/2^+$	→	$23/2^+$	$M1/E2$	b
385.0(0.5)	1.7(0.2)		$31/2^+$	→	$29/2^+$	$M1/E2$	b
388.4(0.5)	75.4(2.7)	0.53(5), [a]0.65(3) [b]	$11/2^-$	→	$9/2^+$	$E1$	y
394.0(0.5)	3.2(0.2)		$29/2^+$	→	$27/2^+$	$M1/E2$	b
408.0(0.5)	1.9(0.2)		$33/2^+$	→	$31/2^+$	$M1/E2$	b
415.0(0.5)	2.1(0.2)		$35/2^+$	→	$33/2^+$	$M1/E2$	b
423.3(1.0)	0.3(0.2)		$35/2^+$	→	$33/2^+$	$M1/E2$	2
439.6(0.5)	1.6(0.2)		$37/2^+$	→	$35/2^+$	$M1/E2$	b
463.0(0.5)	1.7(0.2)		$39/2^+$	→	$37/2^+$	$M1/E2$	b
473.0(1.0)	1.2(0.1)		$41/2^+$	→	$39/2^+$	$M1/E2$	b
485.0(1.0)	0.7(0.1)		$43/2^+$	→	$41/2^+$	$M1/E2$	b
505.8(1.0)	0.3(0.2)		$41/2^+$	→	$39/2^+$	$M1/E2$	1
514.0(1.0)	0.3(0.2)		$45/2^+$	→	$43/2^+$	$M1/E2$	b
516.6(0.5)	2.5(0.2)		$31/2^-$	→	$27/2^-$	$E2$	s
525.0(1.0)	0.3(0.2)		$47/2^+$	→	$45/2^+$	$M1/E2$	b
530.8(0.5)	100.0(3.4)	[d]	$15/2^-$	→	$11/2^-$	$E2$	y
541.0(1.0)	0.2(0.2)		$49/2^+$	→	$47/2^+$	$M1/E2$	b
565.7(0.5)	31.7(0.2)	0.9(1) [b]	$9/2^+$	→	$7/2^+$	$M1/E2$	
582.0(0.5)	19.8(0.8)	0.91(15), [a]1.02(8) [b]	$35/2^-$	→	$31/2^-$	$E2$	s
589.2(1.0)	0.4(0.1)		$45/2^+$	→	$43/2^+$	$M1/E2$	1
604.3(0.5)	1.2(0.2)		$27/2^+$	→	$23/2^+$	$E2$	2
616.0(1.0)	0.2(0.1)		$49/2^+$	→	$47/2^+$	$M1/E2$	1
629.1(0.5)	2.1(0.3)		$27/2^+$	→	$23/2^+$	$E2$	2
629.2(0.5)	47.6(0.1)	1.0(1) [a]	$9/2^+$	→	$5/2^+$	$E2$	
637.7(0.5)	94.8(3.1)	0.97(8), [a]0.99(5) [b]	$19/2^-$	→	$15/2^-$	$E2$	y
670.7(1.0)	0.8(0.2)		$29/2^+$	→	$25/2^+$	$E2$	1
683.6(0.5)	78.7(2.5)	0.94(10), [a]0.97(5) [b]	$23/2^-$	→	$19/2^-$	$E2$	y
685.6(0.5)	2.4(0.6)	1.0(2) [b]	$31/2^+$	→	$27/2^+$	$E2$	2
690.4(0.5)	20.0(0.2)	0.98(4) [b]	$11/2^+$	→	$7/2^+$	$E2$	a
705.4(0.8)	0.7(0.2)		$13/2^+$	→	$9/2^+$	$E2$	b
705.6(0.5)	12.9(0.9)	1.02(6) [b]	$27/2^-$	→	$23/2^-$	$E2$	3
714.5(0.5)	32.4(1.2)	1.09(12), [a]0.97(9) [b]	$35/2^-$	→	$31/2^-$	$E2$	s
717.6(0.5)	3.1(0.3)		$15/2^+$	→	$11/2^+$	$E2$	b
735.5(0.5)	52.7(1.7)	0.94(12), [a]1.01(8) [b]	$39/2^-$	→	$35/2^-$	$E2$	s
736.8(1.0)	0.8(0.6)		$33/2^+$	→	$29/2^+$	$E2$	1
744.0(1.0)	2.7(0.5)		$17/2^+$	→	$13/2^+$	$E2$	b
744.4(1.0)	2.8(0.6)	0.95(8) [b]	$19/2^+$	→	$15/2^+$	$E2$	b
747.0(1.0)	2.7(0.4)		$21/2^+$	→	$17/2^+$	$E2$	b
750.0(1.0)	2.4(0.5)		$23/2^+$	→	$19/2^+$	$E2$	b
755.0(1.0)	1.4(0.5)		$25/2^+$	→	$21/2^+$	$E2$	b

TABLE I. (*Continued*).

E_γ (keV)	I_γ (%)	DCO ratio	I_i^π	→	I_f^π	Multipolarity	Band
755.4(1.0)	2.4(0.7)		$27/2^+$	→	$23/2^+$	$E2$	*b*
756.0(0.5)	10.7(0.7)		$31/2^-$	→	$27/2^-$	$E2$	3
764.8(0.5)	41.8(1.3)	0.93(14), [a]1.03(10) [b]	$43/2^-$	→	$39/2^-$	$E2$	*s*
764.8(0.5)	2.3(0.4)	1.0(2) [b]	$35/2^+$	→	$31/2^+$	$E2$	2
769.0(1.0)	1.3(0.2)		$29/2^+$	→	$25/2^+$	$E2$	*b*
774.3(1.0)	1.7(0.2)		$9/2^+$	→	$7/2^+$	$M1/E2$	
775.0(1.0)	1.1(0.2)		$13/2^+$	→	$9/2^+$	$E2$	*b*
779.0(1.0)	2.4(0.2)		$31/2^+$	→	$27/2^+$	$E2$	*b*
793.0(1.0)	1.3(0.2)		$33/2^+$	→	$29/2^+$	$E2$	*b*
800.6(0.5)	42.7(1.4)	0.97(12), [a]1.04(9) [b]	$31/2^-$	→	$27/2^-$	$E2$	3
806.6(0.6)	2.6(0.4)		$27/2^-$	→	$23/2^-$	$E2$	*s*
818.6(1.0)	0.8(0.2)		$37/2^+$	→	$33/2^+$	$E2$	1
823.0(1.0)	1.4(0.4)		$35/2^+$	→	$31/2^+$	$E2$	*b*
825.7(0.5)	61.8(2.0)	0.92(12), [a]1.05(10) [b]	$27/2^-$	→	$23/2^-$	$E2$	*y*
831.3(1.0)	0.4(0.1)		$35/2^+$	→	$31/2^+$	$E2$	2
838.0(1.0)	1.6(0.2)		$9/2^+$	→	$5/2^+$	$E2$	
841.9(0.5)	2.2(0.2)	[e]	$39/2^+$	→	$35/2^+$	$E2$	2
846.0(0.5)	2.7(0.2)		$9/2^+$	→	$7/2^+$	$M1/E2$	*b*
848.6(0.5)	10.4(1.0)	1.01(6) [b]	$23/2^-$	→	$19/2^-$	$E2$	3
849.1(1.0)	0.5(0.2)		$39/2^+$	→	$35/2^+$	$E2$	2
854.6(1.0)	1.3(0.1)		$37/2^+$	→	$33/2^+$	$E2$	*b*
862.8(0.5)	19.5(1.4)	1.09(6) [b]	$15/2^+$	→	$11/2^+$	$E2$	*a*
867.2(0.5)	10.1(0.5)	0.93(9) [b]	$35/2^-$	→	$31/2^-$	$E2$	3
870.9(0.6)	2.2(0.5)		$27/2^-$	→	$23/2^-$	$E2$	3
884.0(0.5)	7.5(0.4)	[c]	$23/2^+$	→	$19/2^+$	$E2$	*a*
889.1(0.5)	3.9(0.2)		$31/2^-$	→	$27/2^-$	$E2$	*s*
893.1(0.5)	0.9(0.2)		$41/2^+$	→	$37/2^+$	$E2$	1
901.9(0.5)	6.7(0.3)		$39/2^-$	→	$35/2^-$	$E2$	3
902.6(1.0)	0.7(0.2)	0.97(9) [b]	$39/2^+$	→	$35/2^+$	$E2$	*b*
905.6(0.5)	21.1(0.7)	0.96(10) [b]	$51/2^-$	→	$47/2^-$	$E2$	*s*
909.4(0.5)	1.6(0.2)		$9/2^+$	→	$5/2^+$	$E2$	*b*
922.1(0.5)	3.1(0.2)	1.0(2) [b]	$43/2^+$	→	$39/2^+$	$E2$	2
933.9(0.5)	13.4(0.7)	0.92(18), [a]1.00(8) [b]	$31/2^-$	→	$27/2^-$	$E2$	*s*
936.0(1.0)	1.1(0.1)		$41/2^+$	→	$37/2^+$	$E2$	*b*
951.3(0.5)	1.1(0.1)		$45/2^+$	→	$41/2^+$	$E2$	1
958.0(1.0)	0.3(0.2)		$43/2^+$	→	$39/2^+$	$E2$	*b*
968.6(0.5)	32.3(1.0)	0.97(14), [a]1.08(10) [b]	$47/2^-$	→	$43/2^-$	$E2$	*s*
983.0(0.5)	5.8(0.3)	0.98(9) [b]	$43/2^-$	→	$39/2^-$	$E2$	3
983.0(1.0)	0.2(0.1)		$45/2^+$	→	$41/2^+$	$E2$	1
984.5(1.0)	0.5(0.2)		$13/2^+$	→	$9/2^+$	$E2$	*b*
999.0(1.0)	1.0(0.2)		$45/2^+$	→	$41/2^+$	$E2$	*b*
1003.6(0.5)	3.1(0.2)	1.0(2) [b]	$47/2^+$	→	$43/2^+$	$E2$	2
1024.7(0.5)	12.0(0.4)	1.09(10) [b]	$55/2^-$	→	$51/2^-$	$E2$	*s*
1031.3(0.5)	1.6(0.2)		$49/2^+$	→	$45/2^+$	$E2$	1
1039.0(1.0)	0.5(0.2)		$47/2^+$	→	$43/2^+$	$E2$	*b*
1046.9(0.5)	3.0(0.2)		$47/2^-$	→	$43/2^-$	$E2$	3
1066.0(1.0)	0.3(0.2)		$49/2^+$	→	$45/2^+$	$E2$	*b*
1068.3(0.5)	20.1(0.9)	1.03(6) [b]	$19/2^+$	→	$15/2^+$	$E2$	*a*
1073.0(0.5)	2.8(0.2)		$51/2^+$	→	$47/2^+$	$E2$	2
1081.7(0.5)	2.3(0.4)		$23/2^+$	→	$19/2^+$	$E2$	2
1086.1(1.0)	1.2(0.2)		$(57/2^-)$	→	$(53/2^-)$	$E2$	5
1098.0(1.0)	1.1(0.2)		$(57/2^-)$	→	$(53/2^-)$	$E2$	5

TABLE I. (*Continued*).

E_γ (keV)	I_γ (%)	DCO ratio	I_i^π	→	I_f^π	Multipolarity	Band
1098.5(0.5)	3.2(0.2)		$47/2^-$	→	$43/2^-$	$E2$	3
1103.0(0.5)	1.6(0.2)		$53/2^+$	→	$49/2^+$	$E2$	1
1107.3(0.5)	1.2(0.4)		$23/2^+$	→	$19/2^+$	$E2$	2
1120.1(0.9)	2.0(0.2)		$23/2^-$	→	$19/2^-$	$E2$	*s*
1120.8(1.0)	1.7(0.4)		$(61/2^-)$	→	$(57/2^-)$	$E2$	5
1147.7(0.5)	2.2(0.2)		$55/2^+$	→	$51/2^+$	$E2$	2
1149.1(0.3)	2.4(0.2)		$51/2^-$	→	$47/2^-$	$E2$	3
1173.7(1.0)	1.4(0.2)		$(65/2^-)$	→	$(61/2^-)$	$E2$	5
1177.4(1.0)	1.8(0.2)		$57/2^+$	→	$53/2^+$	$E2$	1
1184.1(1.0)	0.8(0.2)		$(61/2^-)$	→	$(57/2^-)$	$E2$	4
1200.4(0.5)	1.9(0.1)		$51/2^-$	→	$47/2^-$	$E2$	3
1212.5(1.0)	0.5(0.1)		$(57/2^+)$	→	$(53/2^+)$	$E2$	7
1235.5(1.0)	0.5(0.2)		$(63/2^-)$	→	$(59/2^-)$	$E2$	6
1239.0(1.0)	0.3(0.1)		$(57/2^+)$	→	$(53/2^+)$	$E2$	7
1249.1(1.0)	0.5(0.1)		$59/2^+$	→	$55/2^+$	$E2$	2
1257.4(1.0)	0.7(0.2)		$(65/2^-)$	→	$(61/2^-)$	$E2$	4
1258.0(1.0)	0.3(0.1)		$(57/2^+)$	→	$(53/2^+)$	$E2$	7
1259.4(1.0)	1.7(0.2)		$61/2^+$	→	$57/2^+$	$E2$	1
1270.5(0.5)	1.9(0.1)		$55/2^-$	→	$51/2^-$	$E2$	3
1295.1(1.0)	1.0(0.1)		$(61/2^+)$	→	$(57/2^+)$	$E2$	7
1299.9(1.0)	0.3(0.2)						5
1331.4(1.0)	0.6(0.1)		$63/2^+$	→	$59/2^+$	$E2$	2
1340.6(1.0)	0.6(0.1)		$(69/2^-)$	→	$(65/2^-)$	$E2$	4
1344.0(1.0)	0.6(0.2)		$(67/2^-)$	→	$(63/2^-)$	$E2$	6
1344.8(1.0)	1.3(0.2)		$(69/2^-)$	→	$(65/2^-)$	$E2$	5
1347.9(1.0)	1.6(0.2)		$65/2^+$	→	$61/2^+$	$E2$	1
1352.9(1.0)	1.5(0.2)		$59/2^-$	→	$55/2^-$	$E2$	3
1360.6(1.0)	0.2(0.1)		$(59/2^+)$	→	$(55/2^+)$	$E2$	9
1380.7(1.0)	1.0(0.1)		$(65/2^+)$	→	$(61/2^+)$	$E2$	7
1394.6(1.0)	0.3(0.2)						5
1410.0(2.0)	0.3(0.2)		$(73/2^-)$	→	$(69/2^-)$	$E2$	5
1426.6(1.0)	0.5(0.1)		$67/2^+$	→	$63/2^+$	$E2$	2
1431.4(1.0)	0.2(0.1)						5
1434.4(1.5)	1.3(0.2)		$63/2^-$	→	$59/2^-$	$E2$	3
1438.5(1.5)	1.3(0.2)		$67/2^-$	→	$63/2^-$	$E2$	3
1441.9(1.0)	1.3(0.2)		$69/2^+$	→	$65/2^+$	$E2$	1
1443.0(1.5)	0.8(0.2)		$71/2^-$	→	$67/2^-$	$E2$	3
1447.8(1.0)	1.2(0.2)		$(73/2^-)$	→	$(69/2^-)$	$E2$	5
1453.4(1.0)	0.5(0.1)		$(71/2^-)$	→	$(67/2^-)$	$E2$	6
1457.1(1.0)	0.6(0.1)		$(73/2^-)$	→	$(69/2^-)$	$E2$	4
1455.9(1.0)	11.1(1.1)		$59/2^-$	→	$55/2^-$	$E2$	*s*
1478.4(1.0)	0.3(0.1)		$(63/2^+)$	→	$(59/2^+)$	$E2$	9
1493.0(1.0)	0.2(0.1)		$(73/2^-)$	→	$(69/2^-)$	$E2$	4
1504.5(1.0)	0.9(0.1)		$(69/2^+)$	→	$(65/2^+)$	$E2$	7
1525.5(1.0)	0.4(0.1)		$71/2^+$	→	$67/2^+$	$E2$	2
1543.7(1.0)	0.3(0.1)		$(67/2^-)$	→	$(63/2^-)$	$E2$	8
1544.8(1.0)	1.2(0.2)		$73/2^+$	→	$69/2^+$	$E2$	1
1554.0(1.0)	0.8(0.2)		$75/2^-$	→	$71/2^-$	$E2$	3
1579.2(1.0)	0.4(0.1)		$(67/2^+)$	→	$(63/2^+)$	$E2$	9
1591.2(1.0)	0.5(0.1)		$(75/2^-)$	→	$(71/2^-)$	$E2$	6
1593.3(1.0)	0.9(0.2)		$(77/2^-)$	→	$(73/2^-)$	$E2$	5
1627.1(1.0)	0.6(0.1)		$(77/2^-)$	→	$(73/2^-)$	$E2$	4

TABLE I. (*Continued*).

E_γ (keV)	I_γ (%)	DCO ratio	I_i^π	→	I_f^π	Multipolarity	Band
1629.6(1.0)	0.3(0.1)		$(71/2^-)$	→	$(67/2^-)$	$E2$	8
1638.2(1.0)	0.4(0.1)		$75/2^+$	→	$71/2^+$	$E2$	2
1651.8(1.0)	1.1(0.2)		$77/2^+$	→	$73/2^+$	$E2$	1
1662.7(1.0)	0.5(0.1)		$(73/2^+)$	→	$(69/2^+)$	$E2$	7
1680.4(1.0)	0.7(0.2)		$79/2^-$	→	$75/2^-$	$E2$	3
1680.5(1.0)	0.2(0.1)		$(81/2^-)$	→	$(77/2^-)$	$E2$	10
1684.3(1.0)	0.3(0.1)		$(71/2^+)$	→	$(67/2^+)$	$E2$	9
1731.4(1.0)	0.4(0.1)		$(79/2^-)$	→	$(75/2^-)$	$E2$	6
1742.2(1.0)	0.3(0.1)		$(75/2^-)$	→	$(71/2^-)$	$E2$	8
1758.4(1.0)	0.5(0.1)		$(81/2^-)$	→	$(77/2^-)$	$E2$	5
1766.9(1.0)	0.9(0.2)		$81/2^+$	→	$77/2^+$	$E2$	1
1767.7(1.0)	0.4(0.1)		$79/2^+$	→	$75/2^+$	$E2$	2
1770.9(1.0)	0.3(0.1)		$(75/2^+)$	→	$(71/2^+)$	$E2$	9
1778.1(1.0)	0.3(0.1)		$(85/2^-)$	→	$(81/2^-)$	$E2$	10
1786.4(1.0)	0.4(0.0)		$(81/2^-)$	→	$(77/2^-)$	$E2$	4
1844.2(1.0)	0.4(0.1)		$83/2^-$	→	$79/2^-$	$E2$	3
1866.9(1.0)	0.3(0.1)		$(79/2^-)$	→	$(75/2^-)$	$E2$	8
1869.7(1.0)	0.3(0.1)		$(77/2^+)$	→	$(73/2^+)$	$E2$	7
1870.6(1.0)	0.4(0.1)		$(89/2^-)$	→	$(85/2^-)$	$E2$	10
1895.8(1.0)	0.6(0.2)		$85/2^+$	→	$81/2^+$	$E2$	1
1905.8(1.0)	0.3(0.1)		$(83/2^-)$	→	$(79/2^-)$	$E2$	6
1915.3(1.0)	0.3(0.1)		$83/2^+$	→	$79/2^+$	$E2$	2
1923.6(1.0)	2.1(0.3)		$63/2^-$	→	$59/2^-$	$E2$	*s*
1944.0(1.0)	0.2(0.1)		$(79/2^+)$	→	$(75/2^+)$	$E2$	9
1970.8(1.0)	0.3(0.0)		$(85/2^-)$	→	$(81/2^-)$	$E2$	4
1972.1(1.0)	0.4(0.1)		$(93/2^-)$	→	$(89/2^-)$	$E2$	10
1984.1(1.0)	0.2(0.1)		$87/2^-$	→	$83/2^-$	$E2$	3
2003.2(1.0)	0.2(0.1)		$(85/2^-)$	→	$(81/2^-)$	$E2$	5
2039.4(2.0)	0.3(0.1)		$(83/2^-)$	→	$(79/2^-)$	$E2$	8
2039.9(1.0)	0.4(0.1)		$89/2^+$	→	$85/2^+$	$E2$	1
2046.6(2.0)	0.2(0.1)		$87/2^-$	→	$83/2^-$	$E2$	3
2049.0(2.0)	0.1(0.1)		$(87/2^-)$	→	$(83/2^-)$	$E2$	6
2075.8(1.0)	0.2(0.1)		$87/2^+$	→	$83/2^+$	$E2$	2
2101.2(2.0)	0.3(0.1)		$(97/2^-)$	→	$(93/2^-)$	$E2$	10
2112.3(2.0)	0.1(0.1)		$(83/2^+)$	→	$(79/2^+)$	$E2$	9
2113.1(2.0)	0.1(0.1)		$(87/2^-)$	→	$(83/2^-)$	$E2$	6
2118.9(2.0)	0.2(0.1)		$(81/2^+)$	→	$(77/2^+)$	$E2$	7
2156.9(2.0)	0.2(0.2)		$(89/2^-)$	→	$(85/2^-)$	$E2$	4
2181.6(2.0)	0.1(0.1)		$91/2^-$	→	$87/2^-$	$E2$	3
2201.0(1.0)	0.2(0.1)		$93/2^+$	→	$89/2^+$	$E2$	1
2202.9(2.0)	0.2(0.1)		$(87/2^-)$	→	$(83/2^-)$	$E2$	8
2241.2(2.0)	0.2(0.1)		$91/2^+$	→	$87/2^+$	$E2$	2
2244.5(2.0)	0.1(0.1)		$91/2^-$	→	$87/2^-$	$E2$	3
2256.7(2.0)	0.2(0.1)		$(101/2^-)$	→	$(97/2^-)$	$E2$	10
2296.9(2.0)	0.1(0.1)		$(89/2^-)$	→	$(85/2^-)$	$E2$	5
2363.0(2.0)	0.1(0.1)		$(89/2^-)$	→	$(85/2^-)$	$E2$	5
2379.5(2.0)	0.2(0.1)		$97/2^+$	→	$93/2^+$	$E2$	1
2426.6(2.0)	0.1(0.1)		$95/2^+$	→	$91/2^+$	$E2$	2
2432.7(2.0)	0.1(0.1)		$(105/2^-)$	→	$(101/2^-)$	$E2$	10
2442.2(2.0)	0.1(0.1)		$95/2^-$	→	$91/2^-$	$E2$	3
2581.1(2.0)	0.1(0.1)		$(99/2)^+$	→	$95/2^+$	$E2$	2
2582.0(2.0)	0.2(0.1)		$(101/2)^+$	→	$97/2^+$	$E2$	1

[a]DCO ratio from backed target experiment.
[b]DCO ratio from thin target experiment.
[c]Gate for band-*a* DCO analysis in thin target experiment.
[d]Gate for band-*y* DCO analysis.
[e]Gate for band-2 DCO analysis.

TABLE II. Band intensities at $E_\gamma \sim 1.6$ MeV.

Band	1	2	3	4	5	6	7	8	9	10
E_γ [keV]	1652	1638	1680	1627	1593	1591	1663	1630	1579	1681
Intensity [%]	1.1(2)	0.4(1)	0.7 (2)	0.6(1)	0.9(2)	0.5(1)	0.5(1)	0.3(1)	0.4(1)	0.2(1)

$\sim 744-$keV gate are consistent with an $M1/E2$ multipolarity. These conclusions are further supported by additional DCO-ratio measurements with gates set on the mixed $M1/E2$ transitions of band *b* (the results of these measurements are not listed in Table I).

B. Bands 1 and 2

Experimental spectra for bands 1 and 2 are shown in Fig. 3. Both bands were reported as unlinked bands 1 and 2 in Ref. [2] with slightly different γ-ray energies. The possible origin of this difference is discussed in Sec. II. Compared to the previous study, bands 1 and 2 were extended to higher spin by one and two transitions, respectively. Good sensitivity of the current thin-target data set resulted in the identification of a number of transitions which extends both bands to lower spins. The fact that the bands could be followed down in spin was essential for linking them to the ground state.

Band 2 decays mainly to the low-spin positive-parity band *a*, as shown in Fig. 2 and in the lower panel of Fig. 3. The spectrum shown in the lower panel of Fig. 3 also indicates the existence of the linking transitions between band 2 and band *b*. Three interband γ rays with energies 423, 831, and 849 keV were isolated between band 2 and band *b* using double and triple gating. The agreement between energy sums for the various decay paths observed in the feeding out of band 2 confirms both the linking of band 2 to the ground state and the decay scheme deduced for band *b*. In addition to the links discussed above, a decay path between band 2 and band *y* exists, as implied by the spectrum shown in the lower panel of Fig. 3. Despite various gating attempts this decay path was not identified in the current study.

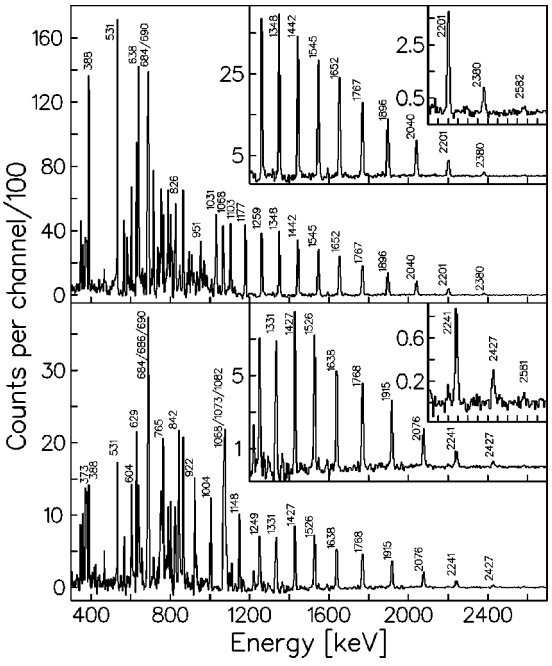

FIG. 3. Experimental spectra presenting bands 1 (top) and 2 (bottom). Double gates set on the $3p$-gated cube were summed to increase the statistics.

DCO analyses for intraband transitions of band 2 were performed using the thin-target data set. Stretched $E2$ multipolarities for the 686-, 765-, 922-, and 1004-keV γ rays are consistent with the DCO ratios extracted in the 842-keV gate. Spin assignments and positive parity as shown in Fig. 2 are proposed for band 2. The decay of band 2 to band *b* can be explained by the close proximity of the $35/2^+$ band members, which are observed to be only 8 keV apart. In the current study, linking transitions between band 2 and band *b* are understood as a consequence of the accidental mixing of these $35/2^+$ states which are built on different single-particle configurations. From the relative level energies it is inferred that the strength of the residual interaction which admix bands 2 and *b* is less then 4 keV. This small interaction strength is consistent with the observation that no other levels of bands 2 and *b* are admixed except for the two $35/2^+$ states.

Band 1, which becomes yrast above spin $\sim 30\ \hbar$, is the most intense high-spin band observed in the current study (see Fig. 3 and Table II). The decay out of band 1, however, contrary to the decay of band 2, is fragmented at low spin over a number of parallel paths. The spectrum shown in Fig. 4 defines the existence of a 589-keV linking transition between bands 1 and 2. The other identified links are a 616-keV transition between bands 1 and 2, and 506- and 983-keV transitions between bands 1 and *b*. The spectrum in the upper panel of Fig. 3 shows that band 1 has significant decay to band *y*, although these paths were not resolved in the current study.

Interband transitions which link band 1 to band 2 near spin $I^\pi \sim 45/2^+$ suggest that these could be signature partners. The spin and parity assignments given to band 1, that are based on this assumption, are presented in Fig. 2. As a consequence of the close proximity of the $41/2^+$ and $45/2^+$ states of bands 1 and *b*, additional linking is observed between bands 1 and *b* because of accidental mixing. An interaction between these states, which are 33 and 16 keV apart, respectively, results in the 506-keV and 983-keV interband transitions. The strength of the residual interaction, which is less then 8 keV as deduced from the relative energies of the $45/2^+$ states, compares well with the related strength for bands 2 and *b* at spin $35/2^+$. This observations give additional confidence to the positive parity and the spins assigned for band 1 in the current study.

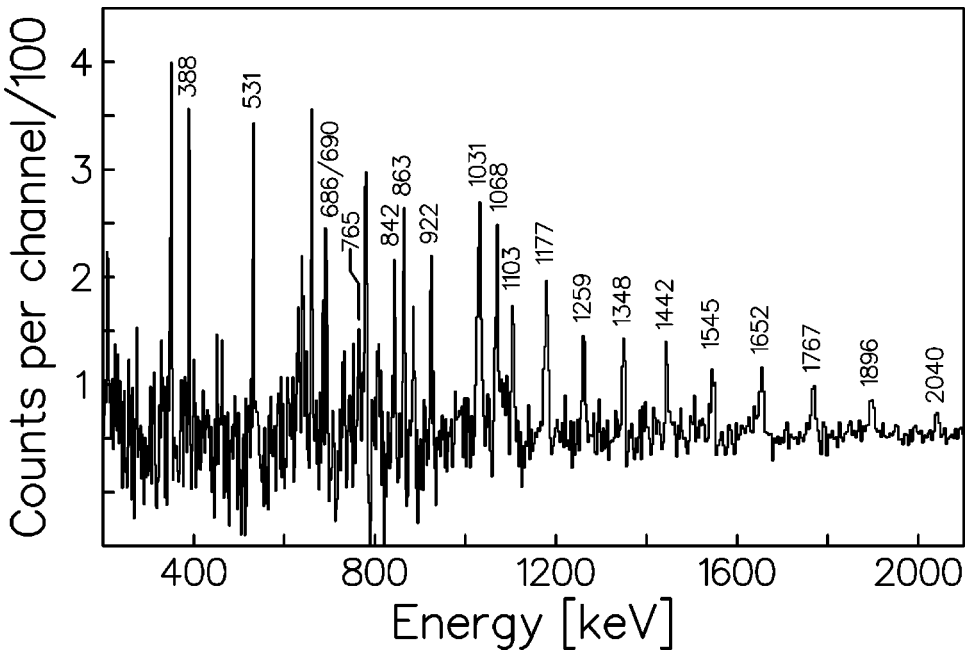

FIG. 4. Experimental spectrum defining the 589-keV linking transition between bands 1 and 2. Double gates with the first gate set on 589-keV γ ray and the second gate set on the intraband transitions in band 1 were summed to increase statistics. Note that the 922-, 842-, and 765-keV transitions of band 2 and transitions of band 1 with energy 1031 keV and higher are observed in the spectrum while transitions of band 2 above 922 keV and transitions of band 1 below 1031 keV are not.

C. Band 3

An experimental spectrum presenting band 3 is shown in Fig. 5. Band 3 of the current study was reported as the linked band 3 in Ref. [2], although the decay scheme and spin assignment proposed there does not fully agree with the current results. At spins $I^{\pi} \sim 31/2^{-}$, the current decay scheme is confirmed by a number of transitions observed between band 3 and bands *s* and *y* (see Fig. 2), which were isolated using double and triple gating. At higher spins (see Fig. 1), the results of three- and four-fold analysis suggest the existence of a triplet at energies 1434, 1439, and 1443 keV, rather than a doublet at 1432 and 1441 keV, as proposed in Ref. [2]. This conclusion is further supported by the large intensity observed in the peak at energy ~1440 keV in the spectrum shown in Fig. 5.

The negative parity and spin assignments for states of band 3 are a consequence of the negative parity and spin assignments for bands *y* and *s*. Indeed, the cascade of 715-, 756-, 706-, and 849-keV γ rays, which involves two transitions of band 3, is observed between the $35/2^{-}$ state of band *s* and the $19/2^{-}$ state of band *y*, implying that each of the transitions has stretched $E2$ multipolarity. This conclusion is supported by the DCO ratios measured for the 706-, 715-, and 849-keV γ rays. The results of the DCO analysis are consistent with stretched $E2$ multipolarity for the 867-, 902-, and 983-keV transitions of band 3 above the $31/2^{-}$ state.

D. Unlinked bands 4–10

Experimental spectra representing bands 4–10 are shown in Figs. 6–12, respectively. Bands 4 and 5 of the current

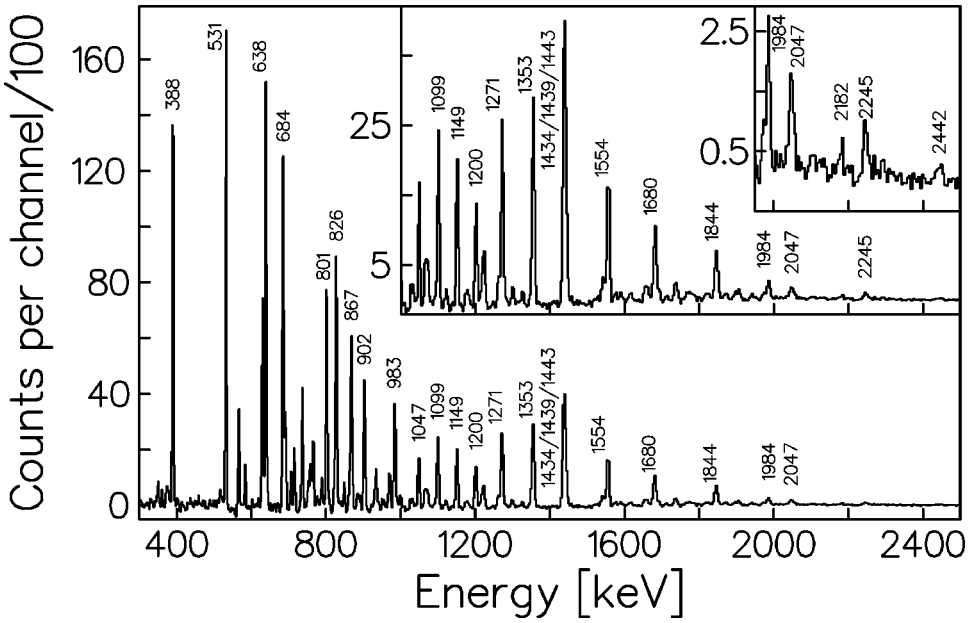

FIG. 5. Experimental spectrum presenting band 3. Double gates set on the $3p$-gated cube were summed to increase the statistics.

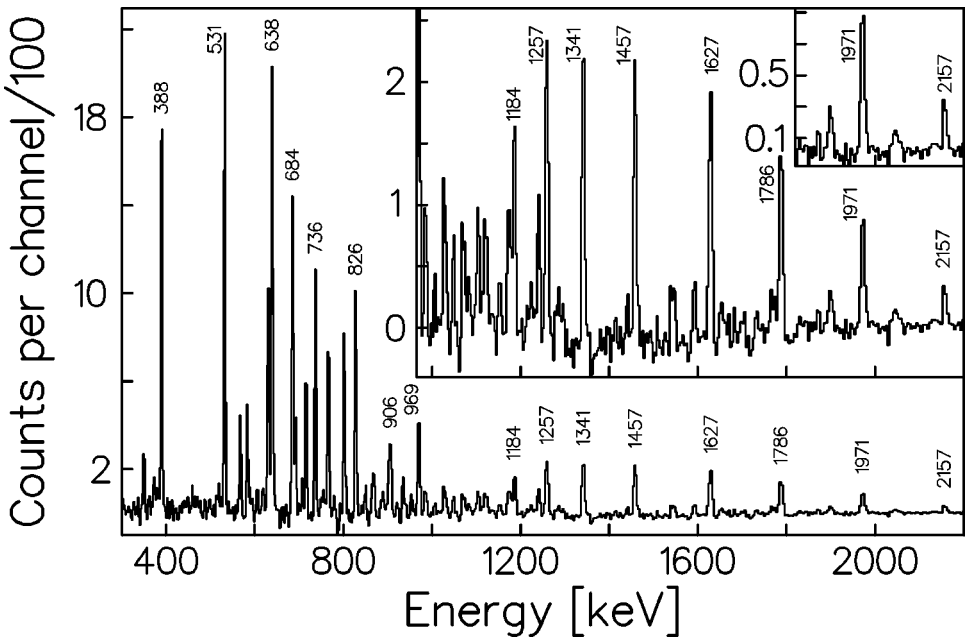

FIG. 6. Experimental spectrum presenting band 4. Double gates set on the $3p$-gated cube were summed to increase the statistics.

study were reported in Ref. [2] as unlinked bands 4 and 5. The level scheme shown in Fig. 1, as well as spectra shown in Figs. 6–12, indicate that the decay out of the lower part of the bands is fragmented over a number of parallel paths. These paths are below the detection sensitivity of the current data set; as a consequence, no discrete transitions were found to link bands 4–10 to the ground state. The data also indicate preferential decay of bands 4–10 to bands *s* and *y*.

The spin assignment for band 5 is based on the theoretical arguments discussed in Sec. IV C which suggest that bands 3 and 5 at high spin are signature partners. Experimentally this conclusion is supported by the comparable intensities observed for bands 3 and 5 (see Table II) and the unresolved decay of band 5 to band 3. The spin assignment for band 4 is a consequence of the assignment proposed for band 5 and the observed cross talk between bands 4 and 5. The transitions connecting bands 4 and 5 are interpreted in the current study as resulting from an accidental mixing between states of both bands which are on the order of 40 keV apart at spin $\sim(73/2^-)$. This suggests the same parity and signature for bands 4 and 5. Spin assignments proposed for bands 6–10 are based entirely on comparisons with the calculations as discussed in Secs. IV C, IV D, and IV E.

IV. DISCUSSION

Experimental data at high spin are compared to the results of configuration-dependent cranked Nilsson-Strutinsky calculations reviewed in Ref. [1]. The calculations discussed in the current paper are identical to those presented in Ref. [2].

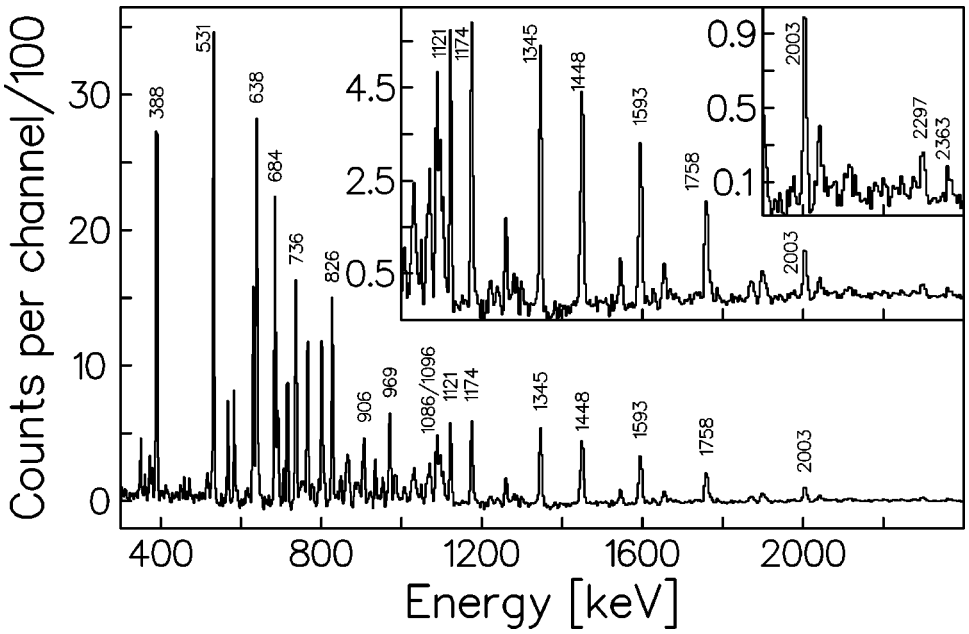

FIG. 7. Experimental spectrum presenting band 5. Double gates set on the $3p$-gated cube were summed to increase the statistics.

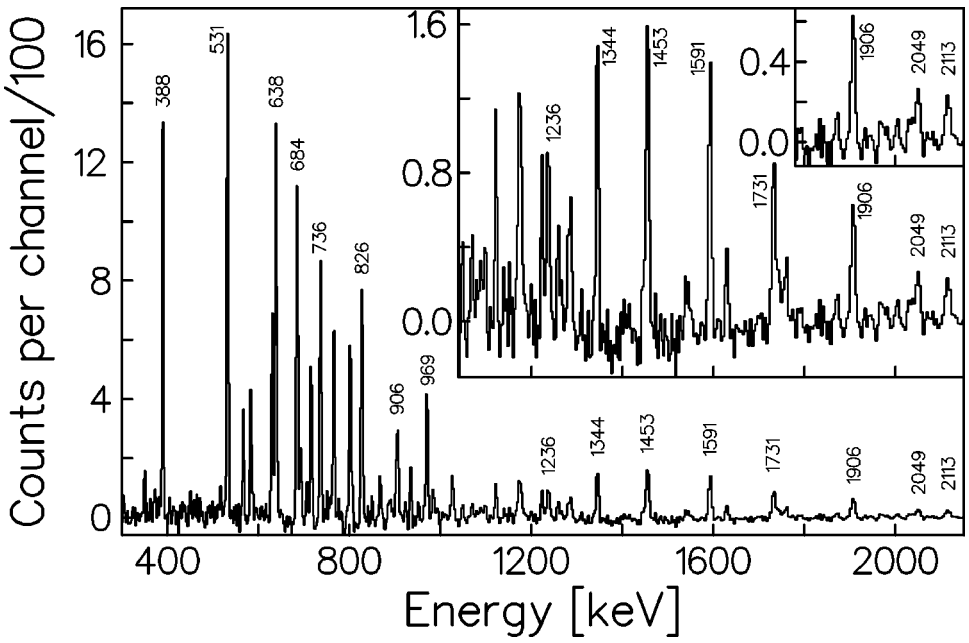

FIG. 8. Experimental spectrum presenting band 6. Double gates set on the $3p$-gated cube were summed to increase the statistics.

The pairing interactions are not accounted for in these calculations, therefore comparisons are valid at high spin above $I \sim 30\ \hbar$, where pairing is expected to play a minor role. It is shown in Sec. IV F, however, that comparisons are still meaningful at moderate spin $I \sim 20\ \hbar$. Calculated yrast and near-yrast bands are presented in Fig. 13 with E-E_{LD} vs angular momentum I plots as defined in Ref. [1]. The four panels correspond to the four possible combinations of parity and signature quantum numbers. The configurations for the bands are marked on the plots following the $[p_1p_2,n_1(n_2n_3)]$ notation, where p_1 is the number of $g_{9/2}$ proton holes, p_2 is the number of $h_{11/2}$ protons, n_1 is the number of $h_{11/2}$ neutrons, n_2 is a number of $g_{9/2}$ or $f_{7/2}$ neutrons, and n_3 is the number of $i_{13/2}$ neutrons. The only observed band with configurations involving the orbitals labeled by n_2 and n_3 is band 10, which possibly has $\nu i_{13/2}$ orbital, therefore in the discussion below the notation is abbreviated to $[p_1p_2,n_1]$ for bands 1–9. The details of the configuration assignments summarized in Table III are discussed below.

A. Bands 1 and 2

Band 1 and band 2 at high spin are identified with the favored signature and unfavored signature of the [22,4] configuration, respectively. This configuration is predicted to be yrast around spin $\sim 50\ \hbar$. The detailed comparisons between calculated and observed energies for states of bands 1 and 2 are shown in Fig. 14. The calculated energies given in Fig. 13 were shifted up arbitrary by a constant value ΔE

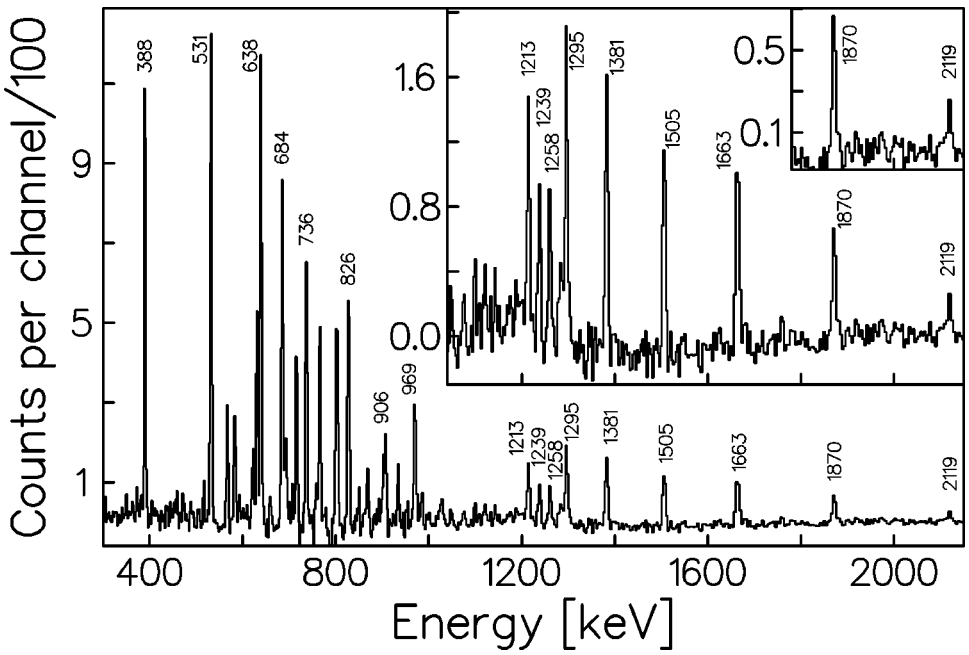

FIG. 9. Experimental spectrum presenting band 7. Double gates set on the $3p$-gated cube were summed to increase the statistics.

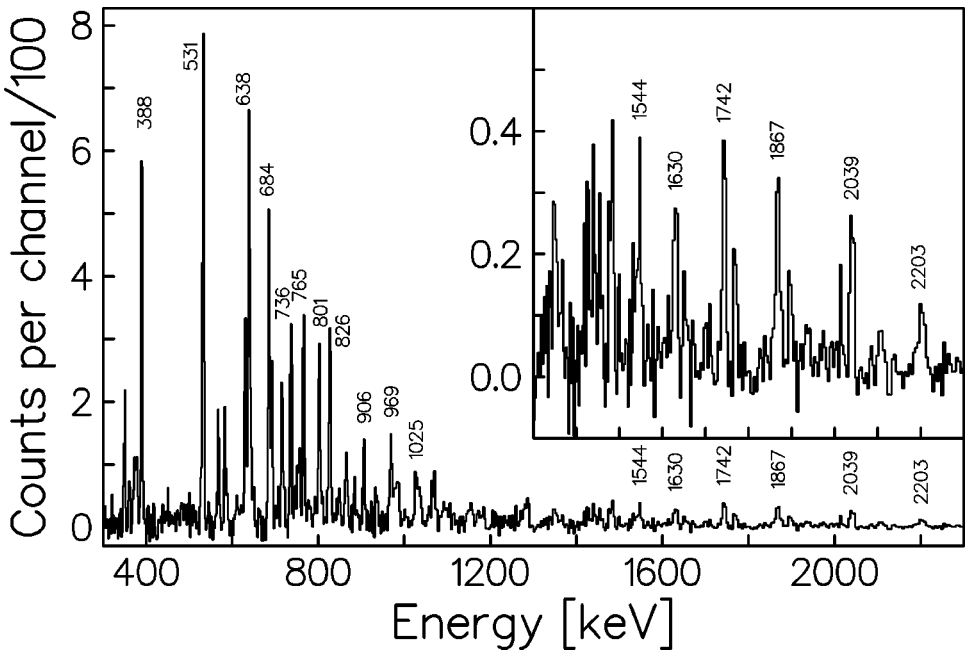

FIG. 10. Experimental spectrum presenting band 8. Double gates set on the $3p$-gated cube were summed to increase the statistics.

$=1.03$ MeV in the Fig. 14 comparison to reproduce the experimental energy of the $93/2^+$ state of band 1. The arbitrary shift is made because the calculations without pairing are not meant to reproduce the properties of the experimental ground state. The shapes of the E-E_{LD} vs I curves for both bands 1 and 2 above spin $\sim 30\ \hbar$ are reproduced remarkably well; with this arbitrary shift band 2 has a ~ -0.5 MeV offset. The positions of the minima for the experimental curves are reproduced with an accuracy better than $1\ \hbar$. Calculations indicate that both bands are observed up to two transitions below the terminating states. As expected, energies for the levels with spin lower than $\sim 30\ \hbar$, which are calculated without the pairing interactions, deviate from those observed in experiment.

Experimental and calculated dynamic moments of inertia for bands 1 and 2, together with the rotating liquid drop moment of inertia for ^{113}I, are shown in Fig. 15. There is no evidence for any sharp backbend at rotational frequencies between $\hbar\omega = 0.5$ and $\hbar\omega = 1.3$ MeV. Moments of inertia for bands 1 and 2 decrease gradually with increasing rotational frequency. At high spin, the dynamic moment of inertia reaches the value equal to approximately half of the value predicted for a rotating liquid drop moment of inertia. This behavior is a characteristic feature of smooth band termination in the mass $A \sim 110$ region. The calculations reproduce the experimental trends with remarkable accuracy.

The transition quadrupole moments (Q_t) calculated according to Eqs. 67 and 69 of Ref. [1] for the [22,4] configu-

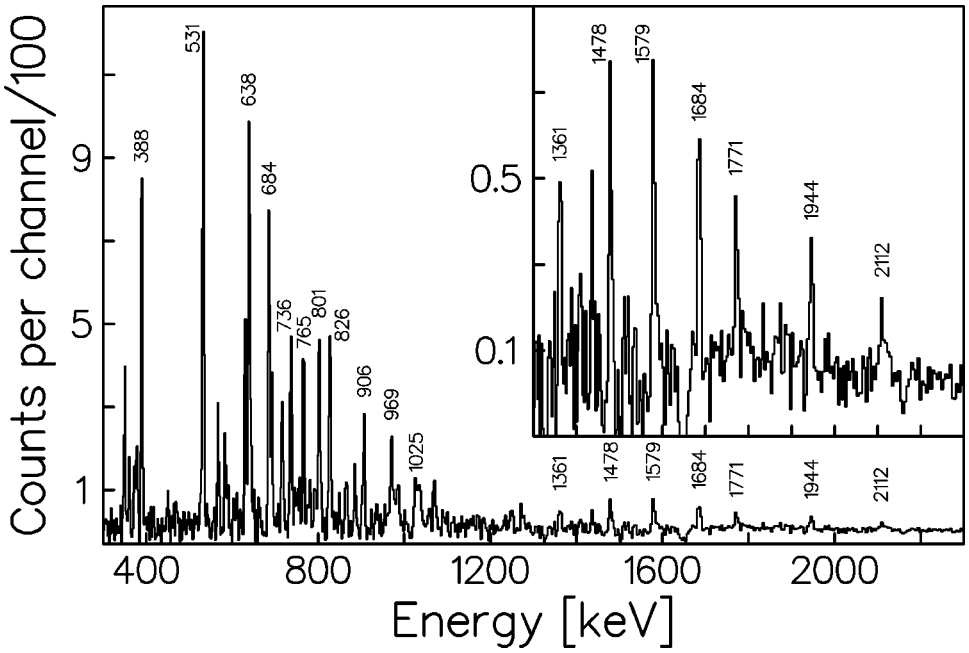

FIG. 11. Experimental spectrum presenting band 9. Double gates set on the $3p$-gated cube were summed to increase the statistics.

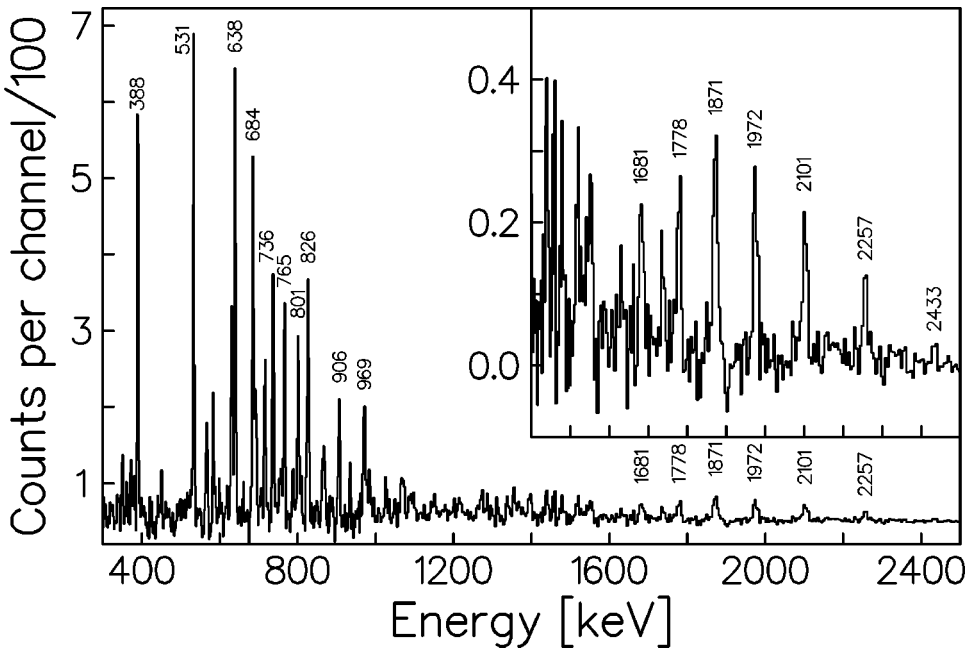

FIG. 12. Experimental spectrum presenting band 10. Double gates set on the $3p$-gated cube were summed to increase the statistics.

ration as a function of angular momentum are shown in the upper panel of Fig. 16. The decreasing trend observed for Q_t as angular momentum increases is explained by the gradual change of the nuclear shape documented on the lower panel of Fig. 16, where a continuous transition in the triaxial plane from the prolate collective ($\gamma=0°$) towards the oblate non-collective ($\gamma=60°$) axis is observed.

B. Band 3

Band 3 at high spin is identified with the favored signature of the [22,3] configuration which is predicted to be yrast around spin $\sim 45\ \hbar$. A detailed comparison between calculated and observed energies for states of band 3 is shown in the upper panel of Fig. 17. The calculated energies were kept at the same arbitrary shift as applied in Fig. 14 to the [22,4] configuration. The agreement of the E-E_{LD} vs I shapes above spin $\sim 30\ \hbar$ is remarkably good; the $\sim$0.5 MeV offset involves the arbitrary shift of the calculated energies. The position of the minimum for the experimental curve is reproduced with accuracy better than $1\ \hbar$. According to the calculation, band 3 is observed up to three transitions below the terminating state.

The calculations indicate that at spin $63/2^-$ the band built on the favored signature of the [22,3] configuration is crossed by the band built on the [00,3] configuration. Below spin $\sim 30\ \hbar$, the data points for band 3 shown in Fig. 17 deviate from those calculated for the [22,3] configuration

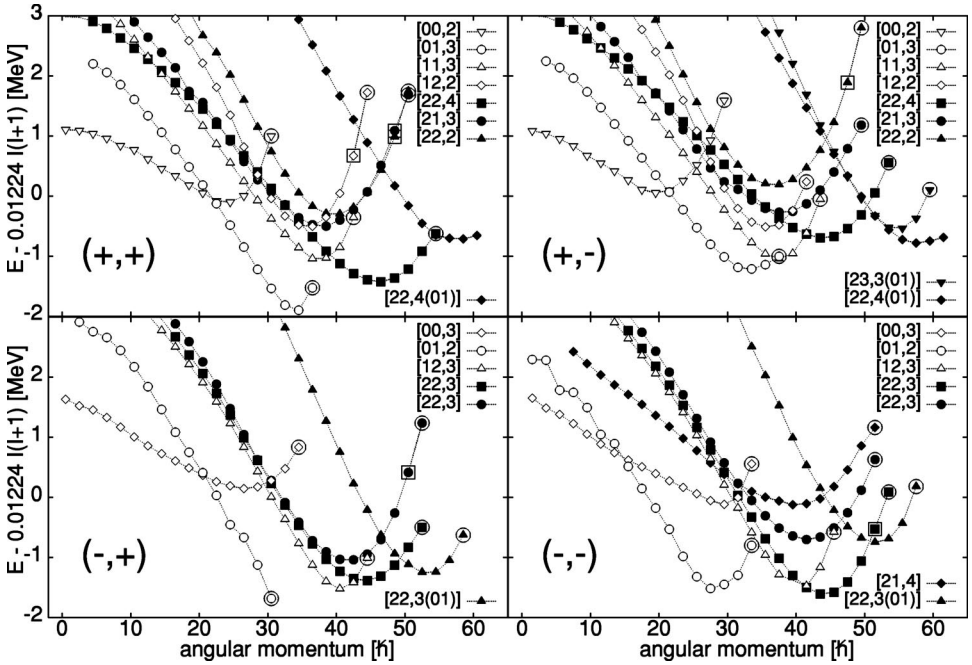

FIG. 13. Calculated E-E_{LD} energies vs angular momentum I for yrast and near-yrast bands from the configuration-dependent cranked Nilsson-Strutinsky approach. The four panels correspond to four possible combinations of parity (π) and signature (α) quantum numbers which are labeled on the plot following (π,α) convention. Large open circles indicate the terminating states, while large open squares indicate the maximum spin values when $\nu d_{3/2}$ and $\nu s_{1/2}$ orbitals are not included into configuration space. See text for the convention used to label the configurations.

TABLE III. Configuration assignment proposed for observed bands.

Band	*y*	*s*	*a*	*b*	1 and 2	3, 4, 5, and 6	7	8	9	10
Conf.	[01,0]	[01,2]	[00,0]	[10,0]	[22,4]	[22,3]	[21,3]	[21,4]	[21,3]	[22,3(01)]

more than expected from the analogous comparison for bands 1 and 2 (see Fig. 14). Band 3 at low spin is interpreted therefore as being built on a configuration which does not involve particle-hole excitation across the $Z=50$ shell gap, but is built instead on a positive-parity proton and three $h_{11/2}$ neutrons. The crossing with a more deformed band is indeed observed at spin $\sim 67/2^-$ and $\hbar\omega \sim 0.7$ MeV as indicated by the sudden increase in the kinematic moment of inertia and large fluctuations in the dynamic moment of inertia shown in the lower panel of Fig. 17. At higher rotational frequencies, the observed decrease of both kinematic and dynamic moments of inertia is consistent with the smooth band termination interpretation as discussed for bands 1 and 2. The trend observed for the dynamic moment of inertia is in very good agreement with the calculations presented in Fig. 15. The kink observed for the dynamic moment of inertia between $\hbar\omega=1.0$ and $\hbar\omega=1.1$ MeV is caused by the accidental mixing observed at spin $87/2^-$, see Fig. 1.

The Q_t values calculated for the [22,3] and [00,3] configurations as a function of angular momentum are shown in the upper panel of Fig. 16. For both configurations the decreasing trend is observed as the angular momentum increases, which is expected from the analysis of calculated nuclear shapes shown in the lower panel of Fig. 16. The transition quadrupole moments and quadrupole deformations are predicted to be smaller for the [00,3] configuration than for the [22,3] and [22,4] configurations where large deformation is induced by the $2p$-$2h$ excitation across the $Z=50$ shell gap. The smaller value of the terminating state spin for [00,3] as compared to those for [22,3] and [22,4] configurations is a consequence of the limited valence space for $0p$-$0h$ compared to that for $2p$-$2h$ configurations. The $E2$ transition lifetimes were calculated for band 3 using experimental γ-ray energies and the Q_t for the [22,3] configuration for states with spin $I^\pi \geqslant 71/2^-$ and Q_t for the [00,3] configuration for states with spin $I^\pi \leqslant 59/2^-$. The smaller transition quadrupole moment for the [00,3] configuration compared to those for to the configurations involving $2p$-$2h$ excitations results in lifetimes at spin $\sim 26\ \hbar$ which are by a factor ~ 3 longer for band 3 compared to those for corresponding states in bands 1 and 2. The proposed [00,3] and [22,3] crossing for band 3 could be tested experimentally through lifetimes measurements using the Doppler shift attenuation method.

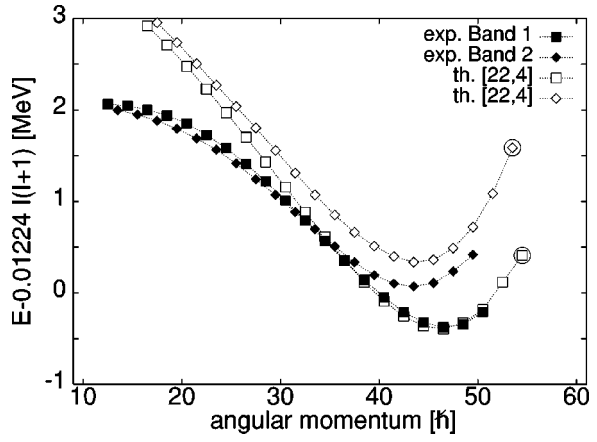

FIG. 14. Comparison between experimental and calculated E-$E_{\rm LD}$ energies as a function of angular momentum for bands 1 and 2.

C. Bands 4, 5, and 6

The good agreement between the data and the calculations for the linked bands, especially the excellent predictions for the position and the curvature near the minima of the E-$E_{\rm LD}$ plots, encourages speculation on configuration assignments for the unlinked bands 4–6 based on the theoretical predictions. For spins $\sim 45\ \hbar$, the calculation predicts four bands

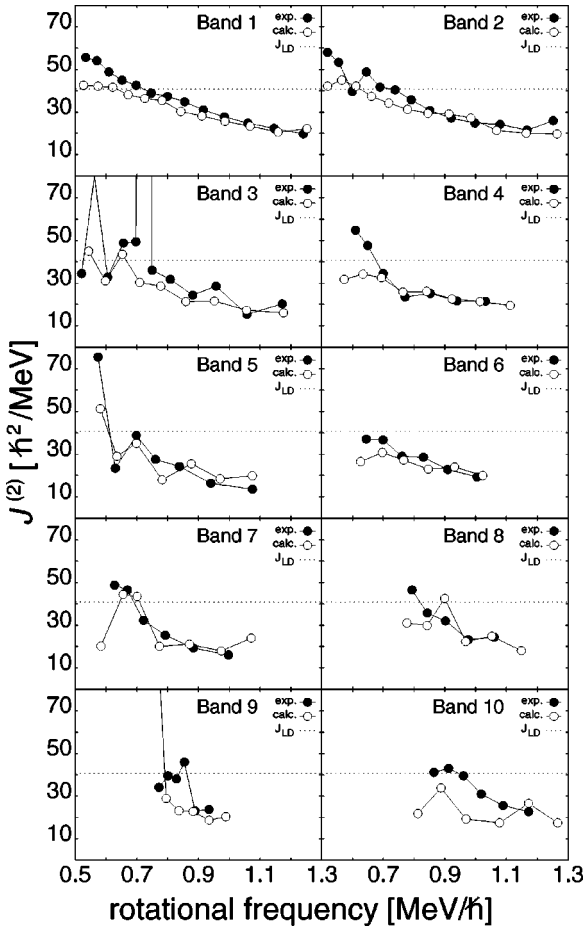

FIG. 15. Experimental and calculated dynamic moments of inertia as a function of rotational frequency for high spin bands in ^{113}I. Small discontinuities in the calculated dynamic moments of inertia are not numerically significant.

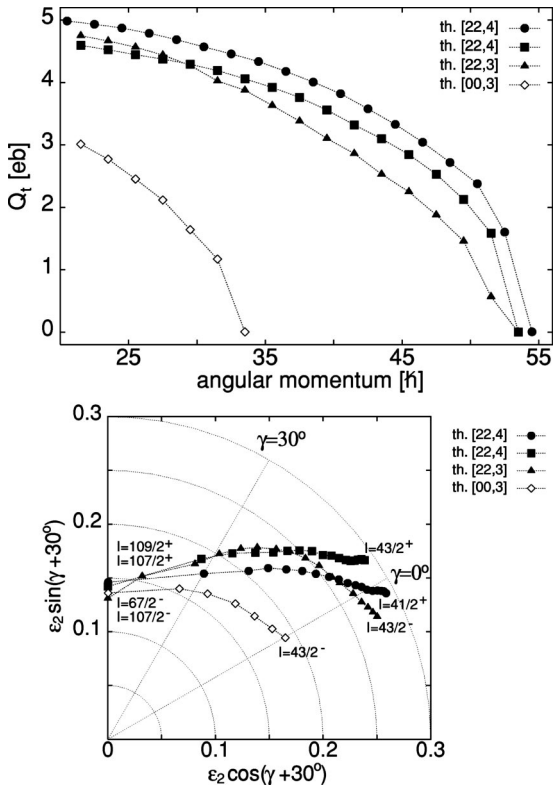

FIG. 16. Top: transition quadrupole moments calculated as a function of angular momentum for selected configurations in ^{113}I. Bottom: equilibrium shapes calculated as a function of angular momentum for selected configurations in ^{113}I. Initial and final spins for each configuration are indicated on the plot. The consecutive data points indicate shapes for states which differ by two units of angular momentum.

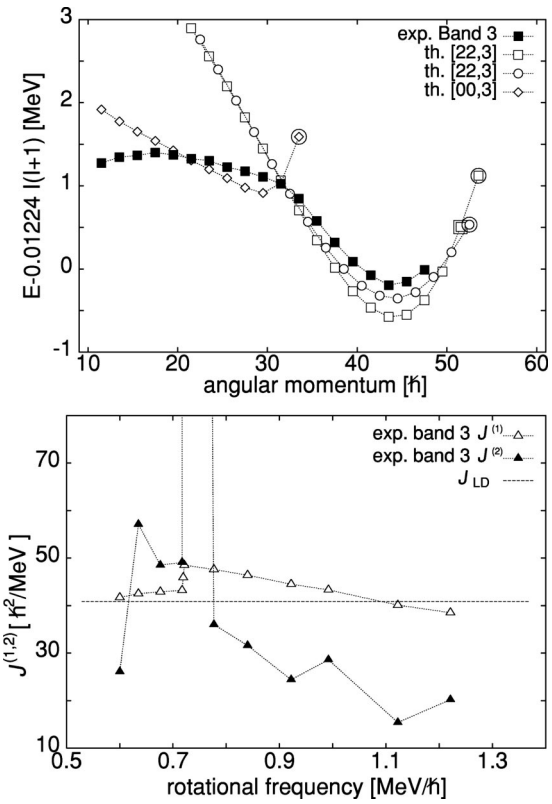

FIG. 17. Top: comparison between experimental and calculated E-E_{LD} energies as a function of angular momentum for band 3. Bottom: experimental kinematic and dynamic moments of inertia as a function of rotational frequency for band 3.

with the [22,3] configuration to exist close to the yrast line (see Fig. 13). These four configurations result from four possible couplings of the two signatures of the proton $(g_{9/2})^{-2}(h_{11/2})^2$ configurations with the two signatures of the $(h_{11/2})^3$ neutron configurations. The two signatures of the proton and two signature of the neutron configurations originate from the occupation of two signatures of the positive-parity $(d_{5/2}g_{7/2})$ orbital. In this sense, four [22,3] configurations can be called signature partners. The lowest-energy, negative-signature [22,3] band was identified in this experiment as band 3 at high spin (see Sec. IV B). The spin and parity assignments proposed for bands 4 and 5 in the current study (see Fig. 1) are based on the assumption that these bands are built on the other signature of the [22,3] configuration. This assignment is rather unique since these bands have the same parity and signature as discussed in Sec. III D and are among the strongest bands observed in the experiment (see Table II). Bands 6 and 7 with comparable intensities (see Table II) are likely candidates for the remaining nonyrast [22,3] band; significantly better agreement between the [22,3] calculation and experimental data is observed, however, for band 6.

Figure 18 shows the comparison between experimental and calculated level energies for bands 3–6 with the spin assignments proposed in Fig. 1. The positions of the minima are well reproduced for all four [22,3] bands. Note that the absolute excitation energy, and as a consequence signature splittings, are not known for these unlinked bands. The absolute energies of the lowest observed levels for bands 5 and 6 were adjusted to reproduce approximately the calculated level energies around spin $\sim$30 $\hbar$. The relative energy be-

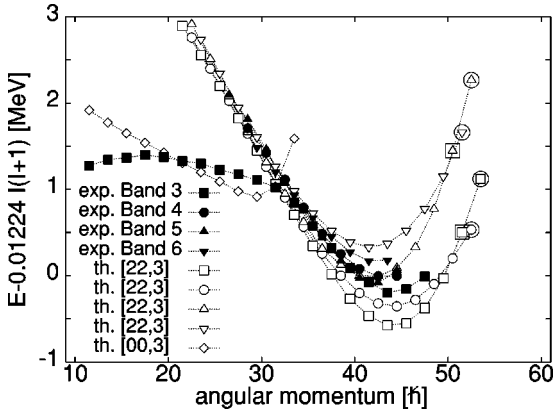

FIG. 18. Comparison between experimental and calculated E-E_{LD} energies as a function of angular momentum for bands 3–6. Unknown absolute excitation energies for unlinked bands 5 and 6 were adjusted to be in approximate agreement with calculations at spin 30 $\hbar$. The relative excitation energy between bands 4 and 5 are determined by their cross talk.

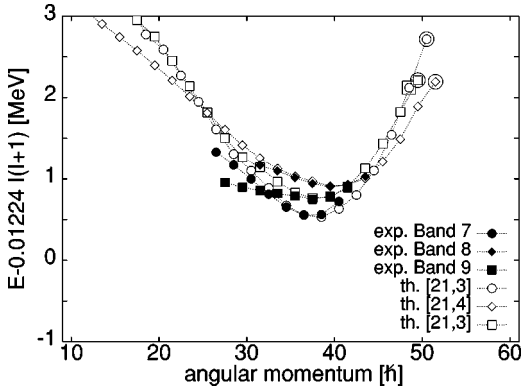

FIG. 19. Comparison between experimental and calculated E-E_{LD} energies as a function of angular momentum for bands 7–9. Unknown absolute excitation energies for unlinked bands 7–9 were adjusted to be in approximate agreement with calculations at the minimum of corresponding E-E_{LD} curves.

tween bands 4 and 5 are determined by their cross talk. Dynamic moments of inertia calculated for bands 4–6 with the [22,3] configuration assignment are in good agreement with the experimental data as presented in Fig. 15.

The trend observed in Fig. 18 for bands 4–6 below spin 30 $\hbar$ differs from that for band 3. The shape of the experimental E-E_{LD} curve for band 3 suggests a crossing between the [00,3] and the lowest energy [22,3] configuration, as discussed in Sec. IV B. There is no experimental evidence for such crossings in bands 4–6, and it is observed that levels of bands 4–6 become very nonyrast below spin 30 $\hbar$ with respect to levels of band 3. The crossing between the [00,3] and the favored [22,3] configuration seems therefore to be a coincidence which allows the band built on the $2p$-$2h$ excitation to be linked to the band with the $0p$-$0h$ excitation and, as a consequence, to the ground state. The decay-out transitions from bands 4–6, on the other hand, are observed to be very fragmented at spins $I \leqslant 30$ and, as a consequence, are difficult to identify.

D. Bands 7, 8, and 9

For the unlinked bands 7, 8, and 9, configurations can again be proposed based on favorable theoretical comparisons as discussed above. Figure 19 shows the comparison between experimental and calculated level energies for bands 7–9 with the spin assignments proposed in Fig. 1. Bands 7 and 8 are in good agreement with calculations for the [21,3] and [21,4] configurations, respectively. This assignment is further supported by the good agreement between calculated and experimental dynamic moments of inertia presented in Fig. 15. Configurations involving $(h_{11/2})^3$ and $(h_{11/2})^4$ neutrons are the basis of intense, linked bands 1–3 and are expected to be favored in ^{113}I at high spin. The proton configurations of bands 7 and 8 differ from those of bands 1–3 by the occupation of a positive-parity $(d_{5/2}g_{7/2})$ orbital rather than one of the negative-parity $h_{11/2}$ orbitals. The low intensity observed in the nonyrast bands 7 and 8 suggest that the position of the proton Fermi level for $Z=53$ at high spin favors configurations with $(h_{11/2})^2$ over $(h_{11/2})^1$ protons.

For band 9, which is proposed as built on the unfavored signature of the [21,3] configuration, the position of the minimum on the E-E_{LD} plot is reproduced reasonably well, although a significant discrepancy between the data and the calculations is observed just below the minimum, at spin 35 $\hbar$, rather than below spin $\sim$30 $\hbar$ as observed for other bands. An alternative assignment investigated for band 9 is the [22,2] configuration with spin $(57/2^+)$ for the lowest state observed in the experiment. The agreement between the calculation and experimental data is comparable for both assignments. It should be noted, that with the discussed configuration assignments, the parity proposed for bands 7 and 9 in the current study is positive; both bands, however, are observed to decay to the negative parity yrast bands *y* and *s* rather than to positive parity bands *a* or *b* (see Figs. 9 and 11). For the above reasons, these configurations possibilities should be considered somewhat speculative.

Configurations proposed for bands 7–9 when drawn as in Fig. 13 are 1–1.5 MeV above the lowest $2p$-$2h$ excitations. There are other bands at a similar energy which are not calculated at present, built, for example, on configurations which involve the unfavored signature when there are an odd number of $h_{11/2}$ protons or neutrons. The signature splitting for the $h_{11/2}$ orbitals in ^{113}I is around 1–1.5 MeV. Thus configurations discussed above for bands 7–9 should be considered as suggestions only.

E. Band 10

The maximum of the intensity profile for a band indicates the frequency at which the band is near the yrast line. In the current study, the intensity profile observed for band 10 peaks at $\hbar\omega \sim 1$ MeV (see Fig. 12); no other band has a maximum at such a high frequency. Band 10 is observed to decay out rapidly at a frequency around $\hbar\omega \sim 0.8$ MeV. This suggests that band 10 is yrast in the highest frequency range observed in the experiment and yet decays out and becomes nonyrast still at a very high frequency. According to calculations presented in Fig. 13, the yrast configurations at spin $\sim$50 $\hbar$ involve a positive-parity $i_{13/2}$ intruder neutron orbital, which originates from the $N=6$ harmonic-oscillator subshell. The intensity profile observed for band 10 suggests that this band may involve the $\nu i_{13/2}$ orbital.

The dynamic moment of inertia observed for band 10 decreases as a function of rotational frequency, as shown in Fig. 15, in agreement with the trend expected for smooth band termination. It consequently stays, however, larger than the dynamic moments of inertia observed for bands 1–3, by a factor of $\sim$20% below $\hbar\omega = 1.0$ MeV, and by a factor of $\sim$10% between $\hbar\omega = 1.0$ and $\hbar\omega = 1.2$ MeV. This observation is consistent with a higher deformation for band 10 with respect to the deformation of bands 1–3, in agreement with expectations for bands involving a deformation-driving $i_{13/2}$ neutron.

The considered $2p$-$2h$ configurations without the $\nu i_{13/2}$ orbital have minima on the E-E_{LD} plot below spin $\sim$45 $\hbar$ as shown in Fig. 13. A spin of at least $\sim$35 $\hbar$ has to be assigned to the lowest observed state in band 10 to achieve a decreasing E-E_{LD} trend with increasing spin below the minimum on

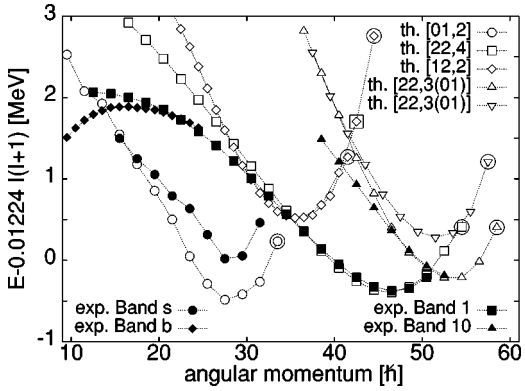

FIG. 20. Comparison between experimental and calculated E-E_{LD} energies as a function of angular momentum for bands 10 and *s*. The data for bands 1 and *b* are plotted for reference purposes.

the E-E_{LD} plot, which is a feature observed for all other bands. With such an assignment, the minimum on the E-E_{LD} plot for band 10 is at spin $\sim$50 $\hbar$ or higher. This strongly supports the configuration assignment including a $\nu i_{13/2}$ orbital for band 10. Figure 20 shows the experimental energies for the states of band 10 with the spin assignments proposed in Fig. 1 to be in very good agreement with those calculated for the favored signature of the [22,3(01)] configuration. The [22,3] portion of the configuration is favored for ^{113}I as discussed for bands 1–6. Band 10 with this interpretation is the first observed band built on configuration including $i_{13/2}$ neutron reported in the $A\sim110$ mass region and is closely related to the superdeformed bands in the $A\sim130$ mass region.

F. Bands *s* and *b*

The negative parity one-quasiparticle band *y* is built on $\pi h_{11/2}$ orbital as discussed in Sec. III A. The three-quasiparticle band *s* is an extension of band *y* after the alignment of an $h_{11/2}$ neutron pair. The frequency of the alignment, $\hbar\omega\sim0.35$ MeV, is well reproduced by cranked Woods-Saxon calculations which include pairing. The low-spin bands are not expected to involve $2p$-$2h$ excitation; therefore a [01,2] configuration assignment is proposed for band *s*. This configuration is the calculated yrast $0p$-$0h$ configuration around $I\sim25$, as shown in Fig. 13. The comparison between the calculation and the experimental data for band *s* presented in Fig. 20 indicates that the unpaired cranked Nilsson-Strutinsky approach can still be applied to states with medium spins $I\sim20\,\hbar$. Indeed, both the energy of band *s* relative to the $2p$-$2h$ band 1, as well as the position of the minimum on the E-E_{LD} plot is reproduced with good accuracy. According to the calculations, band *s* is observed up to one level below the predicted terminating state with spin $67/2^-$.

The positive parity band *b* at low spin is built on a $\pi g_{9/2}^{-1}$ orbital as discussed in Sec. III A. The back bending observed for band *b* at $\hbar\omega\sim0.35$ MeV is attributed to $\nu h_{11/2}$ pair alignment. The [12,2] configuration is expected for band *b* at high spin after the proton $h_{11/2}$ alignment. This configuration is calculated to be nonyrast as shown in Fig. 13 and indeed the intensity of band *b* decreases rapidly after the neutron alignment. A comparison between the calculated and experimental level energies for band *b* is shown in Fig. 20. The experimental data at the highest spin values show the decreasing E-E_{LD} trend as a function of spin, although the intensity in band *b* is lost at spins $I\sim25$, significantly lower than $I\sim35\,\hbar$ where the E-E_{LD} minimum is predicted for the [12,2] configuration.

V. SUMMARY

The structure of ^{113}I has been investigated at high spin following the ^{58}Ni(^{58}Ni,3*p*) reaction. The extensive collective behavior found, was dominated by decoupled rotational bands with significant deformations induced by $2p$-$2h$ excitations across the $Z=50$ shell gap. Ten such bands were observed, compared to five known from the previous study. For three of the ten bands, linking transitions were detected and spins and parities were reliably assigned. The experimental data were compared to calculations based on the configuration-dependent cranked Nilsson-Strutinsky approach. The resulting configuration assignments are unique for the linked bands, while for the unlinked bands, spin and parity assignments were proposed based on these comparisons. The properties of the strongest bands 1–6 were reproduced remarkably well with the six $2p$-$2h$ configurations calculated to be lowest in energy at high spin ($\sim45\,\hbar$). The good agreement achieved for the $0p$-$0h$ bands suggest that the unpaired cranked Nilsson-Strutinsky approach can be applied with reasonable accuracy at moderate spin, $I\sim20$. The current results suggest that the position of the proton Fermi level at high spin in ^{113}I favors configurations with $g_{9/2}^{-2}h_{11/2}^{2}$, while configurations with $h_{11/2}^{3}$ or $h_{11/2}^{4}$ neutrons are about equally favored by the position of the neutron Fermi level. Arguments were presented for one of the $2p$-$2h$ bands to involve an intruder neutron $i_{13/2}$ orbital, which originates from the $N=6$ harmonic-oscillator subshell. This orbital approaches the neutron Fermi level at the highest observed spin and rotational frequency. The current study presents the first evidence for the observation of an $i_{13/2}$ neutron orbital in the $A\sim110$ mass region.

[1] A. V. Afanasjev, D. B. Fossan, G. J. Lane, and I. Ragnarsson, Phys. Rep. **322**, 1 (1999).

[2] M. P. Waring, E. S. Paul, C. W. Beausang, R. M. Clark, R. A. Cunningham, T. Davinson, S. A. Forbes, D. B. Fossan, S. J. Gale, A. Gizon, K. Hauschild, I. M. Hibbert, A. N. James, P. M. Jones, M. J. Joyce, D. R. LaFosse, R. D. Page, I. Ragnarsson, H. Schnare, P. J. Sellin, J. Simpson, P. Vaska, R. Wadsworth, and P. J. Woods, Phys. Rev. C **51**, 2427 (1995).

[3] Gammasphere Proposal, LBNL-PUB-5202; I. Y. Lee, Nucl. Phys. **A520**, 361 (1990).

[4] D. G. Sarantites, P.-F. Hua, M. Devlin, L. G. Sobotka, J. Elson, J. T. Hood, D. R. LaFosse, J. E. Sarantites, and M. R.

Maier, Nucl. Instrum. Methods Phys. Res. A **381**, 418 (1996).
[5] A. J. Boston, E. S. Paul, C. J. Chiara, M. Devlin, D. B. Fossan, S. J. Freeman, D. R. LaFosse, G. J. Lane, M. Leddy, I. Y. Lee, A. O. Macchiavelli, P. J. Nolan, D. G. Sarantites, J. M. Sears, A. T. Semple, J. F. Smith, and K. Starosta, Phys. Rev. C **61**, 064305 (2000).
[6] K. Starosta, C. J. Chiara, D. B. Fossan, T. Koike, D. R. LaFosse, G. J. Lane, J. M. Sears, J. F. Smith, A. J. Boston, P. J. Nolan, E. S. Paul, A. T. Semple, M. Devlin, D. G. Sarantites, I. Y. Lee, and A. O. Macchiavelli, Phys. Rev. C **61**, 034308 (2000).
[7] K. Starosta, D. R. LaFosse, C. J. Chiara, D. B. Fossan, T. Koike, G. J. Lane, J. M. Sears, J. F. Smith, A. J. Boston, P. J. Nolan, E. S. Paul, A. T. Semple, M. Devlin, D. G. Sarantites, I. Y. Lee, and A. O. Macchiavelli, Phys. Rev. C **62**, 044309 (2000).
[8] M. Devlin, L. G. Sobotka, D. G. Sarantites, and D. R. LaFosse, Nucl. Instrum. Methods Phys. Res. A **383**, 506 (1996).
[9] D. C. Radford, Nucl. Instrum. Methods Phys. Res. A **361**, 297 (1995).
[10] A. Krämer-Flecken, T. Morek, R. M. Lieder, W. Gast, G. Hebbinghaus, H. M. Jeger, and W. Urban, Nucl. Instrum. Methods Phys. Res. A **275**, 333 (1989); K. S. Krane, R. M. Steffen, and R. M. Wheeler, Nucl. Data Tables **11**, 351 (1973).
[11] R. M. Steffen and K. Adler, in *The Electromagnetic Interactions in Nuclear Spectroscopy*, edited by W. D. Hamilton (North-Holland, Amsterdam, 1975), Chap. 12.
[12] Ch. Droste, S. G. Rohoziński, K. Starosta, T. Morek, J. Srebrny, and P. Magierski, Nucl. Instrum. Methods Phys. Res. A **378**, 518 (1996).
[13] J. Blachot, Nucl. Data Sheets **83**, 647 (1998).
[14] M. Gai, D. M. Gordon, R. E. Shroy, D. B. Fossan, and A. K. Gaigalas, Phys. Rev. C **26**, 1101 (1982); L. K. Kostov, W. Andrejtscheff, L. G. Kostova, A. Dewald, G. Bohm, K. O. Zell, and P. von Brentano, Z. Phys. A **348**, 79 (1994).
[15] E. S. Paul, D. B. Fossan, K. Hauschild, I. M. Hibbert, P. J. Nolan, H. Schnare, J. M. Sears, I. Thorslund, R. Wadsworth, A. N. Wilson, J. N. Wilson, and I. Ragnarsson, Phys. Rev. C **59**, 1984 (1999).
[16] S. Tormanen, S. Juutinen, R. Julin, A. Lampinen, E. Makela, M. Piiparinen, A. Savelius, A. Virtanen, G. B. Hagemann, Ch. Droste, W. Karczmarczyk, T. Morek, J. Srebrny, and K. Starosta, Nucl. Phys. **A613**, 282 (1997).